3

Indoor Wireless Communications and Applications

Chapter Editor: K. Haneda, Section Editors: W. Joseph, E. Tanghe, A. Bamba, U.-T. Virk, E.-M. Vitucci, C. Gustafson, J.-M. Molina-Garcia-Pardo, K. Witrisal, P. Kulakowski, P. Meissner and E. Leitinger

Chapter 3 addresses challenges in radio link and system design in indoor scenarios. Given the fact that most human activities take place in indoor environments, the need for supporting ubiquitous indoor data connectivity and location/tracking service becomes even more important than in the previous decades. Specific technical challenges addressed in this section are (i), modelling complex indoor radio channels for effective antenna deployment, (ii), potential of millimeter-wave (mm-wave) radios for supporting higher data rates, and (iii), feasible indoor localisation and tracking techniques, which are summarised in three dedicated sections of this chapter.

3.1 Advances in Short-Range Radio System Design

In the forthcoming years, due to the increasing popularity of multiple-input multiple-output (MIMO), massive MIMO and wide- and ultra wideband (UWB) transmission schemes along with the increasing use of small cells, the conventional propagation models will no longer suffice. This section introduces methods for accurate characterisation of channels and advanced channel models, detailing about dense multipath components (DMCs), different channel simulation methods and modelling techniques for MIMO and UWB. Finally, new antenna deployment approaches and their performance are discussed.

3.1.1 Characterisation of the Indoor Channel Using Room Electromagnetics (REM) and Diffuse Multipath

In this subsection, the diffuse components of the indoor channel are characterised using two approaches, namely, high-resolution algorithms and the REM. State-of-the-art REM models to determine the reverberation times will be presented and the contribution of the diffuse multipath components (DMCs) in industry will be determined using RiMAX.

3.1.1.1 Introduction: REM and diffuse multipath components (DMCs)

The radio channel not only consists of specular paths with well-defined *discrete* locations in the different radio channel dimensions (e.g., space, frequency, time, etc.) but also of DMC, which are *continuous* across these dimensions [Ric05, OCD+12]. These not only originate from distributed diffuse scattering on electrically small objects but also include all radio SMCs channel energy that cannot be associated with the due to the inconsistency of the specular multipath model with reality [PSH+11, MQO12]. The dense and SMCs are often also referred to as the incoherent and coherent parts of the radio channel, respectively [ETJ14]. It has been shown that the DMC power density may contribute significantly – up to 95% – to the total power density in an indoor environment [PSH+11]. Two approaches have been proposed to tackle the modelling of DMC in real indoor channels.

The first approach is based on the use of the high-resolution algorithms such as RiMAX, i.e., an iterative maximum-likelihood multipath search algorithm [Ric05]. The specular and DMCs can be estimated from the channel sounding data by means of RiMAX because it is built on a data model that allows for both specular and DMCs. The second modelling approach is based upon the REM [ANP+07]. Basically, the theory states that the PDP of indoor environments is comprised of two parts: the line-of-sight (LoS) signal if any and the diffuse fields. The LoS component (black line in Figure 3.1(a)) is due to the direct propagation between the transceivers. The diffuse fields stem from multiple scattering of the electromagnetic waves on rough surfaces (walls, ceiling, floor, furniture, etc.) and diffractions at corners.

3.1.1.2 REM models

Room electromagnetics modelling is used in [SPF+12, SPF+13a, GSML+14], to characterise the PDP and proposed for multi-link radio channels, UWB channels, the estimation of the absorption cross-section of a person, and hybrid raytracing.
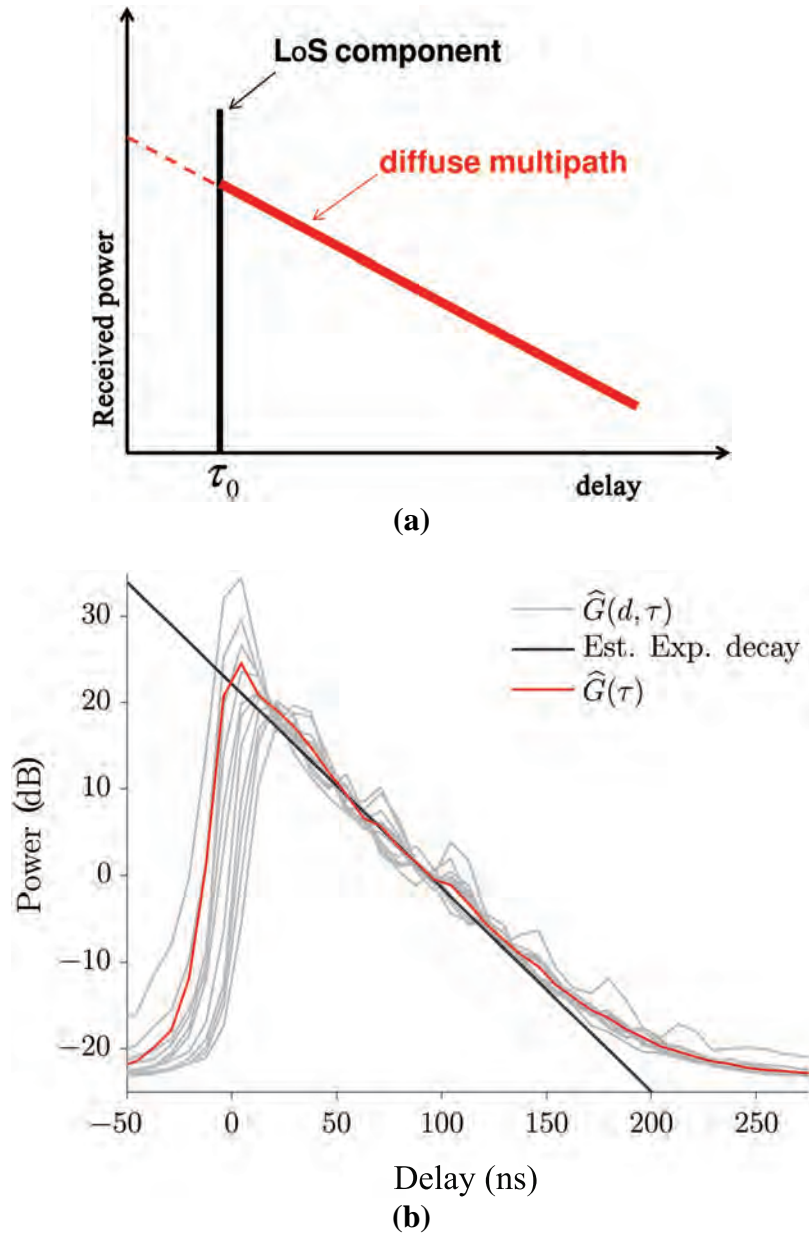
(a)

Delay (ns)

(b)

Figure 3.1   (a) Power delay profile (PDP) modelling according to the room electromagnetics (REM) theory, (b) spatially averaged PDPs obtained for transmitter–receiver distance intervals of 4 λ for receiver positions [SPF$^+$12, SPF$^+$13b].

Steinböck et al. [SPF$^+$13a] validates experimentally the prediction accuracy of reverberation models applied to electromagnetics in typical indoor environments (consisting of different scenarios A–F). The predictions obtained with Sabine's [Sab92, Kut00] and Eyring's [Eyr30, Kut00] models are then compared with the experimental results. The experimental data of Figure 3.1(b) is used to perform the validation. Figure 3.2(a) shows that Sabine's model generally seems to predict too large reverberation times and the prediction error increases when the average absorption coefficient increases. The predictions obtained with Eyring's model shown in Figure 3.2(a) are close to the experimental results and their respective confidence intervals overlap except in Scenario E. The obtained results indicate that the reverberation models are valid for REM and that Eyring's model provides a better prediction. In Steinböck et al. [SPF15], Eyring's model is proposed to estimate the absorption cross-section of a person. The obtained values can be used to predict the change of reverberation time with persons in the propagation environment. This allows prediction of channel characteristics of communication systems in presence of humans.

Bamba et al. [BJT$^+$12, BJT$^+$13] aim to introduce an electrical circuit model based on the REM theory [ANP$^+$07], while Bamba et al. [BMG$^+$14] investigates the electromagnetic reverberation time characteristics as a function of frequency and for UWB. The measurements have been carried out in two laboratories from 2 to 10 GHz. The results demonstrate that, for a given frequency, the reverberation time is constant over a large bandwidth up to 900 MHz. Figure 3.2(b) shows the experimental (*black circles*) and predicted (*blue curve*) reverberation time values from 2 to 10 GHz. Maximum (resp. average) relative errors between the predicted and the measured values are about 22.30% (resp. 8.80%) for the investigated frequency range. These low deviations show that the model accurately predicts the reverberation time values. Figure 3.2(b) also shows the decrease of the reverberation time as the frequency increases. This indicates that the energy is fading faster away at higher frequencies compared to lower frequencies. In addition, the reverberation time decreases smoothly as the frequency increases, indicating that the diffuse fields fade at a faster rate at higher frequencies. This is attributed to the frequency dependence of the absorption coefficient of the building materials.

3.1.1.3 Diffuse multipath components (DMCs) in industry

Lienard et al. [ETJ13, ETJ14] present an analysis of DMC in an industrial workshop for shipping container restoration. Radio channel sounding experiments with a vector network analyser and virtual antenna arrays are carried
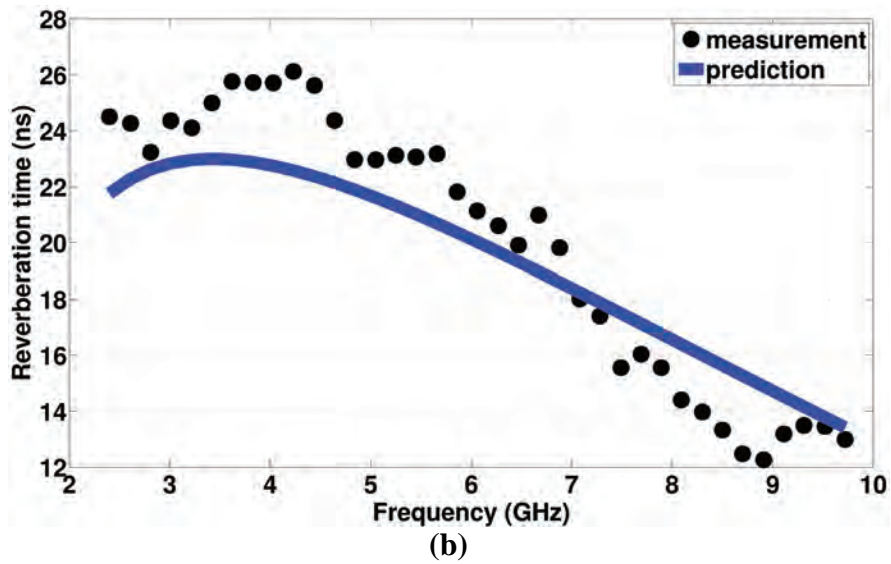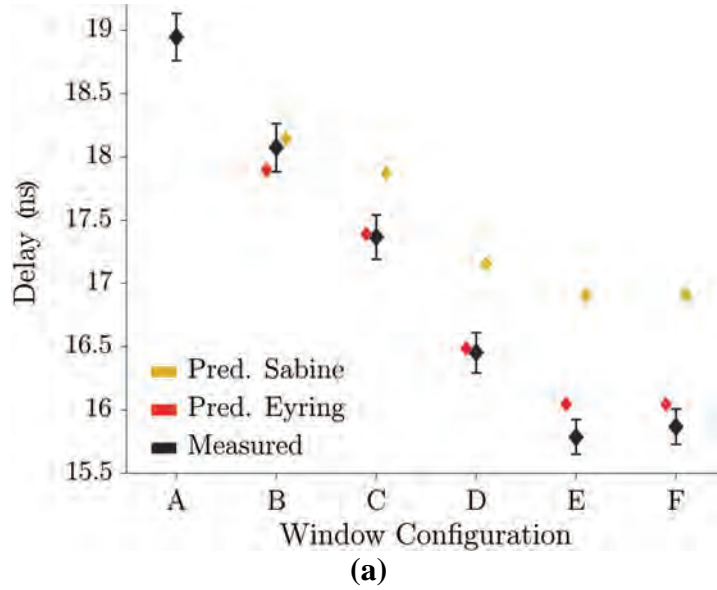
(a)

(b)

Figure 3.2 (a) Estimated and predicted reverberation times. The predictions with Eyring's and Sabine's models for the different scenarios are shown including the 95% confidence interval [SPF$^+$13a], (b) experimental (*black circles*) and model (*blue line*) of τ from 2 and 10, i.e., 2 to 10 GHz.

out. Specular and DMCs are estimated from channel sounding data by means of RiMAX.

In this study of Lienard et al. [ETJ13, ETJ14], the DMC power is found to account for 23–70% of the total channel power. Significant difference between DMC powers in LoS and non-line-of-sight (NLoS) situations is discovered, and this difference can be largely attributed to the power of the LoS multipath component (MPC). Overall, DMC in the industrial workshop appears to be more important than in office environments, i.e., a larger fraction of channel power and longer reverberation times are observed: this is explained by the highly cluttered and metallic nature of the industrial environment. Table 3.1 presents a comparison of the fractional DMC power f_{DMC} with related work in office environments. The work of Poutanen et al. [PSH$^+$11] also found a strong link between f_{DMC} and link shadowing category. The larger f_{DMC} in the industrial environment may be explained by presence of many clutters in the environment leading to diffuse scattering. Additionally, the measurements in Lienard et al. [ETJ13, ETJ14] are performed at a lower centre frequency than in Poutanen et al. [PSH$^+$11].

A comprehensive analysis of the polarisation characteristics of SMCs and DMCs in a large industrial hall based on frequency-domain channel sounding experiments at 1.3 GHz with 22 MHz bandwidth is presented in Tanghe et al. [IV14]. In summary, strong (antenna de-embedded) SMC depolarisation is obtained for the horizontal (H) polarisation in obstructed-line-of-sight (OLoS) scenarios. On the other hand, DMC depolarisation is observed to be weaker than previously reported for indoor environments but constant across LoS/OLoS, polarisation, and distance. Finally, a full-polarimetric distance-dependent model of the PDP for large hall scenarios is proposed in Cheng et al. [CGT$^+$15]. A two-step method is proposed to compute the path loss (PL) exponent of the estimated components from the measured data. This approach provides a deeper understanding of the indoor radio channel when including DMC.

Table 3.1 Fractional DMC power f_{DMC} for industrial and office environments

Reference	Environment	Centre Frequency (GHz)	Link Shadowing (%)		
			LoS	OLoS	NLoS
Poutanen et al. [PSH$^+$11]	Open hall in office building	5.3	10–25	35–65	60–90
Quitin et al. [QOHD10]	Office building	3.6	n/a	20–60	
Lienard et al. [ETJ13, ETJ14]	Industrial workshop	3.0	23–38	27–70	57–64

3.1.2 Characterisation of the Indoor Channel Using Simulations: Heuristic, Ray-based and Full Wave

This subsection introduces various examples of indoor radio channel modelling with different complexity and accuracy. The complexity and accuracy depends on the channel modelling method, such as full-wave methods, ray-tracing and a heuristic method. In case of site-specific channel modelling, the level of modelling accuracy depends on the quality of the environment description. Prospects and limitations of different indoor radio channel modelling approaches are illustrated through concrete example results.

3.1.2.1 Heuristic channel modelling

The work of Plets et al. [PJA+14] uses a heuristic electromagnetic pathloss prediction tool, called a WiCa Heuristic Indoor Propagation Prediction (WHIPP) tool [PJV+12], to evaluate the whole-body exposure due to indoor base station antennas PL or access points in downlink, and localised exposure due to mobile devices in uplink indoor channels. The tool calculates the PL by considering the effect of the environment on the radio channel and by determining a DP between transmitter and receiver, i.e., the path along which the signal encounters the lowest obstruction. The PL and subsequently the link budget estimates are calibrated by an RSS measurements of a commercial mobile phone. The calibration led to 3 dB accuracy in mobile transmit (Tx) power estimates as illustrated in Figure 3.3(a). Using the calibrated power estimates, three phone-call scenarios, i.e., universal mobile telecommunications system (UMTS) macrocell, UMTS femtocell, and WiFi voice-over-IP, are compared with respect to the localised specific absorption rate (SAR) distribution. The benefit of a low localised SAR_{10g} is illustrated in the UMTS uplink scenario due to the power control mechanism.

3.1.2.2 Full-wave channel modelling

The work of Virk et al. [VHK+13] reported characterisation of electromagnetic field propagation inside a room using the finite difference time domain (FDTD) method. Thanks to the advancement of computational power and availability of strong computational unit such as a graphical processing unit, it is possible to run full-wave simulation in a feasible time for a propagation environment with a limited electric volume. The predicted PL using the SEMCAD-X and the corresponding measurement are compared as shown in Figure 3.3(b). It was found that the distance-decaying factor of the PL and the small-scale fading were estimated well, but the absolute power level showed about 5 dB constant offset. Possible reasons behind the offset
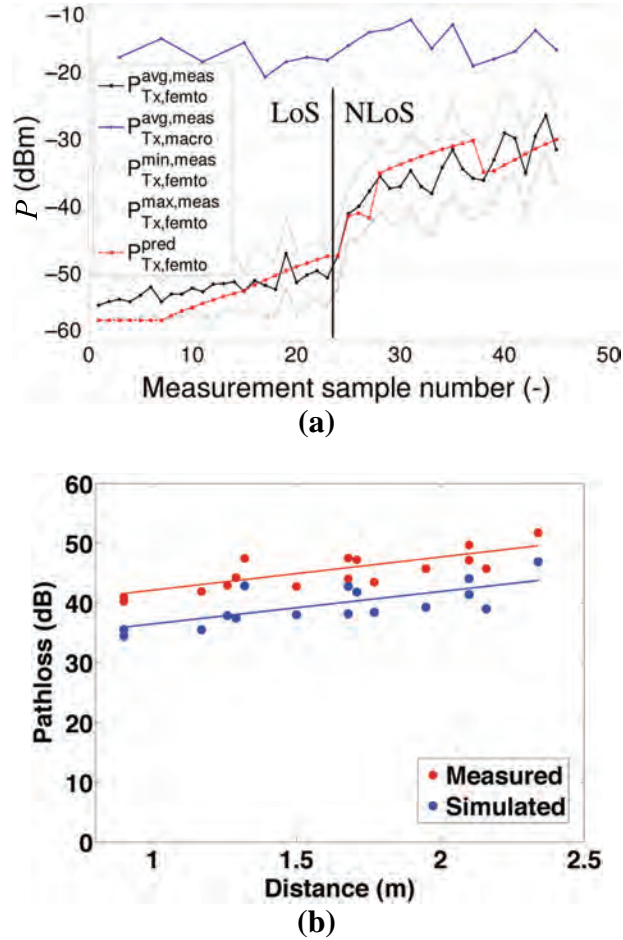
(a)

(b)

Figure 3.3   (a) Measured and predicted uplink power at a mobile, radiated to a femtocell base station at various mobile locations. The greater measurement sample number of the *x*-axis corresponds to greater distance from the base station [PJA$^+$14]. (b) Comparison of path loss (PL) between measurements and finite difference time domain (FDTD) simulation in an office room.

are numerical wave dispersion, conversion of the electric field values to a PL estimate and imperfect absorbing boundary conditions.

The works of Kavanagh and Brennan [BK14] and Kavanagh and Brennan [KB15] report a two-dimensional full-wave solver of electromagnetic wave propagation in indoor environments based on the volume electric field integral equation (VEFIE) formulation. The formulation is in frequency domain and

hence produces a matrix equation when discretised by the method of moments. The matrix equation can be iteratively solved and accelerated by using the fast fourier transform (FFT). The unknown fields are derived only on the scatterers, and those in the free-space were calculated through a simple post-processing to reduce the number of iterations required. Numerical results of electric field distribution in a hypothetical two-dimensional room are compared with the results of the exact solution, showing validity of the VEFIE formulation.

3.1.2.3 Advanced ray-based modelling

One of the key challenges in ray-based indoor channel modelling is acquisition of accurate description of the environment. Available blueprints of the indoor environments may not be sufficient for accurate channel modelling since they often miss necessary details such as fixtures and metallic structures that may reflect or block radio waves.

The work of Vitucci et al. [VFDE14] revealed that a proper description of the propagation environment with an accurate choice of material parameters is a key factor to predict radio channels accurately. A full three-dimensional ray-tracing tool [DEGd$^+$04] is used to predict radio propagation inside a large exhibition hall, with the aim of reproducing root mean square (RMS) delay spread (DS) and angular spread accurately as reality. The peculiarity of the building was highly reflective floors and ceilings due to embedded metal structures and meshes. Figure 3.4(a) shows that inclusion of the reflective floors and ceilings and surrounding buildings is required to predict DSs accurately.

The works of Järveläinen and Haneda [JH1], Virk et al. [VHW14], and Wagen et al. [WVH15] proposed a ray-based channel modelling based on an accurate description of the physical environment, which is obtained from laser scanning, called a point cloud. The challenge in channel modelling based on the point cloud is the fact that there is no predefined surface for calculating specular reflections. The early works of Järveläinen and Haneda [JH1] and Virk et al. [VHW14], therefore, used only diffuse scattering, assuming that each point in the point cloud produces electromagnetic scattering. However, it was demonstrated in Wagen et al. [WVH15] that specular reflections can also be reproduced in addition to the diffuse scattering. The environmental description in the form of the point cloud allows us to analyse the level of structural details that is essential for accurate channel modelling. For example, Virk et al. [VHW14] showed that a simple empty room model suffices to predict PDPs of a small office room. The work compares the PDPs based on the point cloud to those with an empty room model having the same dimension as illustrated
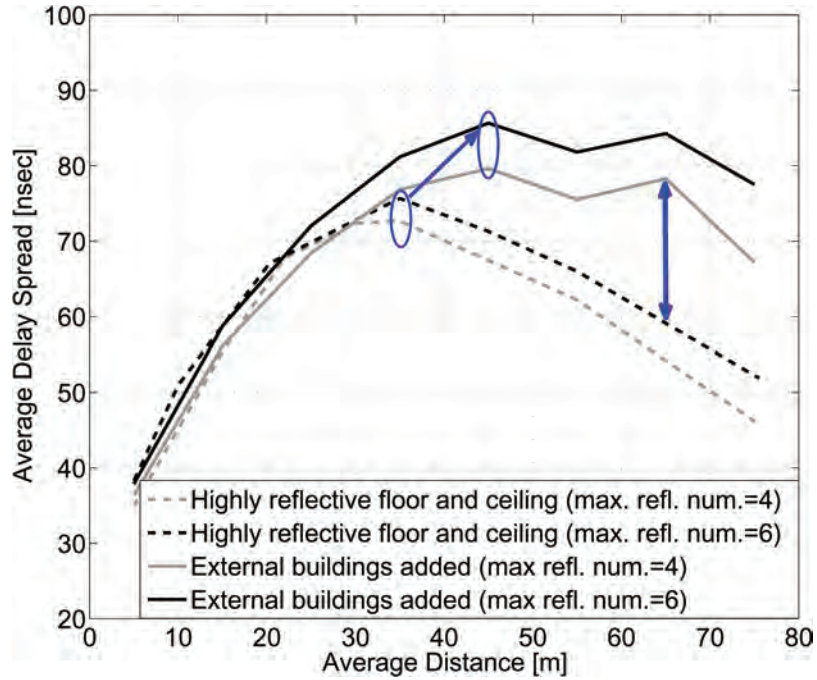
(a)
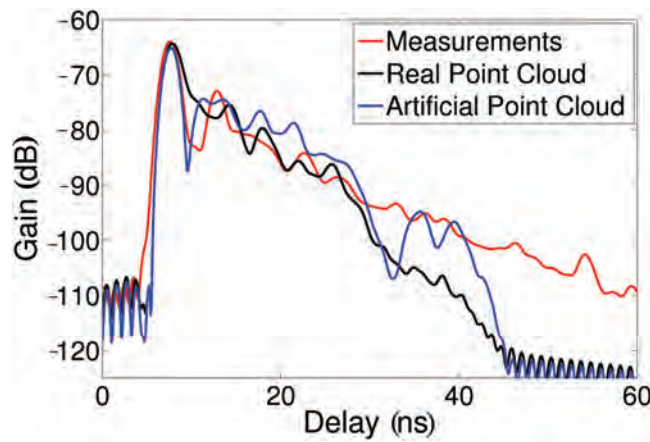
(b)

Figure 3.4 (a) Comparison of delay spreads (DSs) from ray-tracing simulations using two environmental settings; one with highly conductive floor and ceiling and another with surrounding buildings [VFDE14]. (b) Comparison of PDPs between measurements and ray-based channel modelling with accurate environmental description and an empty room model at 10 GHz radio frequency [VHW14].

in Figure 3.4(b). The figure shows a decent agreement of both modelling results to the measurement, because of the dominance of electromagnetic field reverberation inside the room.

3.1.3 Advanced Indoor Propagation Modelling

New advanced techniques for indoor propagation characterisation and modelling are presented in this subsection. Such techniques deal with: (i) spatial, temporal, and polarisation characteristics of multi-antenna and multi-link indoor channels; (ii) time and frequency dependence in UWB indoor channels; and (iii) accurate models for deployment of next-generation mobile networks.

3.1.3.1 Characterisation of multi-antenna and multi-link indoor channels

In Haneda et al. [HTKD11, HKD$^+$13], a method to identify an upper bound of spatial diversity gain in multipath channels is presented. The spatial diversity gain is derived from the measured propagation channels by applying the spherical wavemode expansion method [Han88]. The dependence of the attainable spatial diversity gain for a given array volume is shown in Figure 3.5 for several measurement locations at 6 GHz in an industrial room scenario: the gain increases with the size of the antenna array, and three-times larger diversity gains are achieved in OLoS scenarios compared to LoS scenarios. The attainable diversity gain is less than 3 dB indicating that *any* two-branch antenna array realised in the volume originates correlated signals in the tested propagation environments.

Distributed MIMO, i.e., MIMO with large separation between the elements of the antenna arrays, has been proposed as a solution to exploit the beneficial effect of spatial diversity gains. Actually, its performance is closely related to the low cross-correlation of the large-scale fading between multiple links. In Tian et al. [TZY12], the fading correlations for different Tx antenna configurations are analysed based on measurements data collected in an indoor office environment. It is shown that for some particular configurations, e.g., when the elements of the Tx array are distributed symmetrically with respect to both the receivers (or Rxs) and the propagation environment, the spatial cross correlation (SCC) is non-negligible (i.e., larger than 0.3). In such cases, an additional polarisation diversity can effectively reduce the correlation and enhance the capacity gain, since the joint spatial and polarisation cross correlation (SPCC) is shown to assume negligible values (around 0.1) in most of the considered cases.
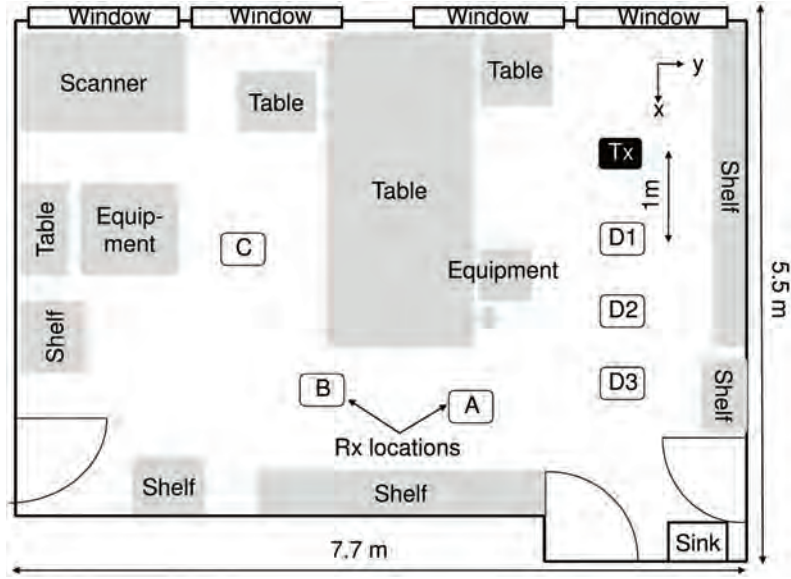
(a)
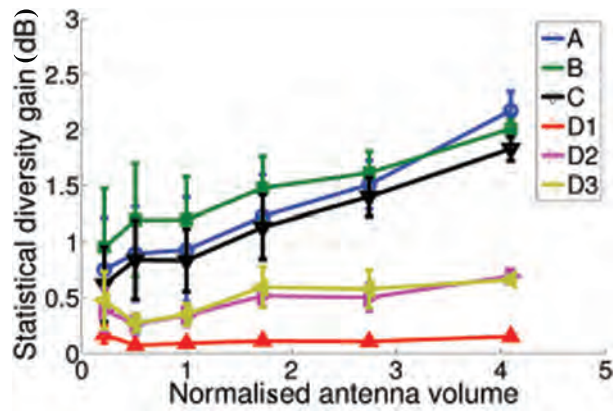
(b)

Figure 3.5   Dependence of the attainable spatial diversity gain against the volume of a cubical hollow array at 6 GHz, in an industrial room scenario [HTKD11].

   In the work of Kim et al. [KKCT12] and Chang et al. [CKKT12], extensive measurement campaigns for wideband MIMO systems at 11 GHz with large arrays are presented. In particular, in Kim et al. [KKCT12], the influence of the polarisation on PL, DS and MIMO capacity is investigated for a 12×4

dual-polarised MIMO system. It is shown that the DS does not significantly depend on the polarisation, while PL is highly degraded in some NLoS locations when the horizontally polarised transmission is used, because of high losses originated by penetration, sidewall reflections, and diffraction on door edges. This leads to a significant degradation of the MIMO capacity, due to the well-known keyhole effect [CO13].

In Chang et al. [CKKT12], measurements with a 8×12 MIMO system in a dynamic scenario with randomly moving people are used to develop a new stochastic model, called 2 dominant paths (2DP) model. In addition to the LoS and stochastic-NLoS components of the well-known Rician MIMO channel model [CO13], an additional term is introduced, the so-called dominant non-line-of-sight (dNLoS) component. According to this model, the MIMO channel matrix for the i-th subcarrier ($\mathbf{H}_i{}^{2DP}$) can be then expressed as:

$$\mathbf{H}_i^{2DP} = \sqrt{\frac{A}{1+A+B}}\mathbf{H}_i^{\mathrm{LoS}} + \sqrt{\frac{B}{1+A+B}}\mathbf{H}_i^{\mathrm{dNLoS}}$$

$$+ \sqrt{\frac{1}{1+A+B}}\mathbf{H}_i^{\mathrm{NLoS}}, \tag{3.1}$$

where the subscript i refers to the i-th subcarrier, $\mathbf{H}_i^{\mathrm{LoS}}$, $\mathbf{H}_i^{\mathrm{dNLoS}}$ and $\mathbf{H}_i^{\mathrm{NLoS}}$, are the channel matrices related the LoS, dNLoS, and NLoS components, and A, B are the power ratios of the LoS and dNLoS to the stochastic NLoS components. The 2DP model better agrees the measurements shown in Chang et al. [CKKT12] compared to the Rician model, while the LoS and dNLoS components are highly correlated to the first and second eigenvalue of the MIMO channel.

A statistical characterisation of fast-fading in indoor peer-to-peer networks based on channel measurements is provided in Vinogradov and Oestges [VO13]. The small-scale fading statistics are evaluated using the second-order scattering fading (SOSF) distribution which reflects any combination of Rician, Rayleigh, and double-Rayleigh fading [CO13]. It is shown that in double mobile scenarios the predominant fading mechanism is a combination of Rayleigh and double-Rayleigh fading, while Rician fading or combinations of LoS and double Rayleigh components are occasionally observed. In single mobile scenarios, fading is either Rician or Rayleigh distributed. These different fading behaviors mainly depend on the mobility of the nodes, and the transitions between them can be described by a hidden Markov model [EM02].

3.1.3.2 Modelling of time and frequency dependence
in UWB indoor channels

In UWB wireless propagation channels, each MPC can exhibit delay dispersion, i.e., frequency dependence. This effect is investigated in Haneda et al. [HRM12], where a method to extract the significant MPCs based on the image principle is presented. Such a method identifies locations and intensity of both original radio sources and image sources. A map of image source distribution is experimentally constructed (Figure 3.6) based on UWB propagation measurements in a small office scenario, with the frequency varying from 3.1 to 10.6 GHz. A detection method is then applied to the map to identify the significant image sources, which are then tracked over different sub-bands to get the frequency dependence of their intensity and location. A MPC-wise frequency dependence model is finally proposed, which can be combined with existing channel models. The effectiveness of this approach is evident in Figure 3.6(c): the inclusion of the frequency dependence characteristics of MPCs in the IEEE802.15.4a channel model [MFP03] reveals noticeable differences in the shape of the channel impulse responses (CIRs), with a considerable impact on UWB radio system design.

In Hanssens [HTM$^+$14], the frequency dependence of Doppler Spread for UWB indoor communication in a time-varying office environment is investigated. A measurement campaign ranging from 3.1 to 10.6 GHz was performed for several days, using a network analyser. Measurements show a clear frequency-dependent behavior: in particular, a heavy decrease of Doppler Spread is observed from 3.1 to 5.1 GHz, followed by a steady behavior up until 8 GHz, and a slight decrease toward 10.6 GHz. Results also confirm that the well-known Jakes' Doppler spectrum no longer applies in such a scenario, in agreement with theoretical predictions shown in Thoen et al. [TdPE02].

### 3.1.3.3 Accurate propagation models for mobile networks
deployment

The increasing traffic demand from inoor users in future mobile communication networks will require the deployment of femto cells to cover areas inside buildings. For this reason, accurate PL models including building penetration losses are needed. An extensive measurement campaign in the ultra high frequency (UHF) band aiming at modelling the indoor-to-outdoor and indoor-to-indoor propagation for long term evolution (LTE) femto cells is described in Giménez et al. [GJRC12] and Ballester et al. [BGJ$^+$13]. In Giménez et al. [GJRC12] measurement results are analysed
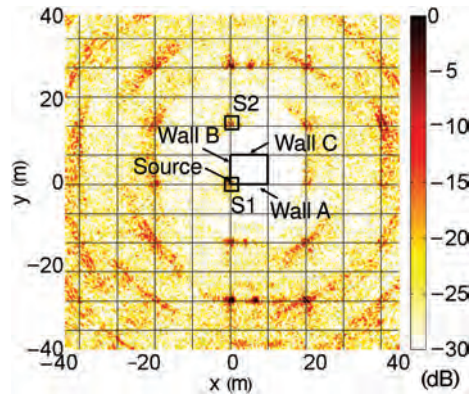
(a)
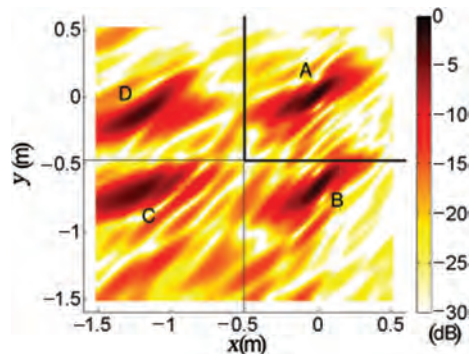
(b)
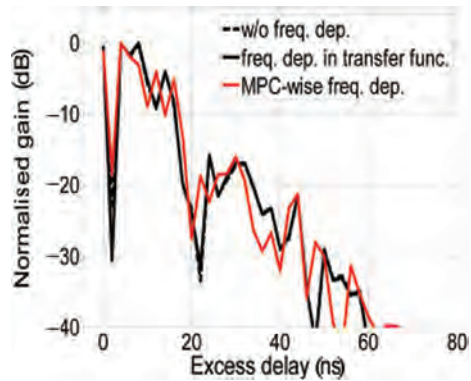
(c)

Figure 3.6 (a) Overall map of image source distribution and (b) enlarged map for the source group S1; and (c) effect of the multipath component (MPC)-wise frequency dependence [HRM12].

with respect to indoor-to-outdoor propagation characteristics, using the model described in Rose et al. [RJK11] as a reference. It is shown in particular that specular reflections from metal structures (e.g., the metal shield of elevators) can give strong contributions, increasing the total RSS. An analysis of the indoor-to-indoor propagation losses in the same measurement scenario is reported in Ballester et al. [BGJ$^+$13]. The COST 231 multi-wall model (MWM) is taken as a reference and new values of the empirical parameters are derived in order to minimise the error relative to measurements, using an optimisation algorithm based on the Nelder–Mead Simplex Method [NM65]. The resultant expression for the model that fits the measurements is the following:

$$L = L_{\text{FS}}(1.83, d) + 41.53 + \sum_{i=1}^{N} 3.98 \cdot K_{\text{wi}} + 15.42 \cdot K_{\text{f}}^{\{\frac{K_{\text{f}}+2}{K_{\text{f}}+1} - 0.48\}} \quad (3.2)$$

where L_{FS} is the free-space attenuation corrected with a proper PL exponent, d is the distance, K_{wi} is number of penetrated walls of type i, and K_{f} is number of penetrated floors. Using this formula, an average estimation error of 0.85 dB and a standard deviation of 4.63 dB are achieved for the measurements shown in Ballester et al. [BGJ$^+$13].

3.1.4 Advanced MIMO Techniques: Leaky Coaxial Cables (LCXs), Distributed Antenna System (DAS) and Massive MIMO

This subsection briefly introduces two techniques for achieving a uniform wireless coverage, namely LCXs and DAS. It is discussed how these techniques can be used in conjunction with MIMO. The implication of massive MIMO on multipath estimation is also discussed in this subsection.

3.1.4.1 LCXs

The use of LCXs as antennas in MIMO wireless communication is discussed in Medbo and Nilsson [MN12]. The main advantage of LCXs in single-antenna systems is a uniform distribution of the signal strength due to the LCX's distributed nature [Mor99]. However, the performance of LCXs in a MIMO setup was largely unknown. A measurement-based analysis of the MIMO mutual information of a 2×2 system in an 80 MHz bandwidth centered at 2.44 GHz is presented in Medbo and Nilsson [MN12]. The receiving antennas are two LCXs of length 20 m and the transmitting antennas are regular electrical dipole and magnetic loop antennas. When the two LCXs are

mounted about 1 m apart, the measurements show that the MIMO capacity is slightly better than that of an independent and identically distributed (i.i.d) MIMO channel. Interestingly, when the two LCXs are taped together, the MIMO capacity is only slightly worse than that of the i.i.d. channel.

3.1.4.2 DAS

Apart from leaky cables, DAS is another way of achieving a more uniform wireless coverage [SRR87]. In a traditional DAS, the same signal is distributed to a number of remote antenna units (RAUs) to achieve a better and more capillary radio coverage. The use of MIMO in conjunction with DAS is discussed in Vitucci et al. [VTF+14]. A straightforward implementation distributes the entire MIMO signal to RAUs equipped with multiple antennas and is called co-located MIMO DAS (c-MIMO DAS). In another implementation called interleaved MIMO DAS (i-MIMO DAS), the different MIMO branches are split up and sent to different RAUs. The advantage of i-MIMO DAS over c-MIMO DAS is that older SISO DAS deployments with single-antenna RAUs can be re-used to implement MIMO. The downside of i-MIMO DAS is that the MIMO branches become spatially well-separated, leading to power imbalances of these branches at the receiver side and thus to capacity losses.

Tian et al. [TNB14a] discuss the uplink error performance of a DAS system where the RAUs are LTE eNodeBs. Maximum-ratio combining (MRC) techniques are applied to the eNodeB signals before sending the combined signal to the LTE base station. Tian et al. [TNB14a] investigate two MRC strategies. The first one is a "space-only" MRC technique that applies different MRC weights to the different eNodeB signals. The second, more complex, "space-frequency" MRC technique is the same but also applies different weights to different frequency carriers. Simulations with the WINNER II channel model [KMH+08] show an expected performance improvement of the space-frequency MRC technique in highly frequency-selective channels. However, the authors argue that complexity of the space-frequency technique may outweigh the performance benefits in practical LTE DAS systems.

3.1.4.3 Massive MIMO

One of the main challenges in radio channel modelling for massive MIMO scenarios is how to ensure the spatial consistency of the model [MBH+14]. Conventional MIMO arrays are compact: it can be readily assumed that each MPC behaves as a plane wave. For massive MIMO arrays, however, the plane wave assumption is difficult to maintain and a spherical wavefront assumption is more appropriate. In the spherical wavefront assumption, the

directions of arrival and departure change for each element of the array. Yin et al. [YWZ14] propose a modification of the space-alternating generalised expectation maximisation (SAGE) MPC estimator [FTH$^+$99] to account for spherical wavefronts. The traditional parameters of each MPC are estimated: the directions of arrival and departure (for a reference antenna), the time-delay, the Doppler frequency, and the full-polarimetric complex amplitudes. To consider spherical wave fronts, two additional parameter dimensions are added: the two distances from Tx to the first bounce point and from the last bounce point to the Rx.

3.2 Towards Higher Frequencies: Millimeter-Wave Radios

With the growing number of wireless devices and the ever increasing demand for higher wireless data rates, next generation wireless systems for cellular and WiFi technology may have to utilise frequency bands that are well above the frequency bands below 6 GHz that are typically used today. Recent developments in RF technology have made it feasible to produce cost-effective radios that operate in different mm-wave frequency bands in the range from 30–300 GHz. With the large amount of underutilised spectrum available in the mm-wave range, this could potentially unlock huge swaths of bandwidth for cellular and WiFi technology.

For indoor short-range high data rate wireless communications, the 60 GHz band has attracted the most attention due to the large amount of unlicensed bandwidth (about 5–9 GHz) available worldwide. For this band, the IEEE802.11ad and IEEE802.15.3c standards has been defined, and commercial products are already available. Besides the unlicensed 60 GHz band, the potential of other frequency bands, such as the 28, 38, 70, and 80 GHz bands, are also being investigated. The frequency bands around 28 and 38 GHz have been pointed out as feasible candidates for next generation cellular technologies, whereas the 60, 70, and 80 GHz bands have been identified as viable candidates for indoor short range wireless communications, such as WiFi and device-to-device technologies.

3.2.1 Comparison with Lower Frequency Bands

Wireless propagation in the mm-wave range is inherently different from propagation in the lower frequency bands commonly used today. The attenuation associated with propagation in the mm-wave range is generally higher compared to lower frequency bands for the following reasons: (i) The free-space

PL is proportional to the square of the carrier frequency (assuming constant-gain antennas), and thus much higher than for the 2 and 5 GHz bands. (ii) The dimensions of physical objects in a room are typically large in relation to the wavelength of about 1–10 mm in the mm-wave range, resulting in sharp shadow zones. (iii) The transmission through obstacles such as walls is much lower compared to lower frequencies.

In Martinez-Ingles et al. [MMP$^+$14], radio wave propagation in the 2–10 and 57–66 GHz bands are compared based on measurements in an indoor laboratory environment under LoS conditions. Metrics such as the PL, DS, coherence bandwidth and Rician K-factor for these two bands are compared. Typical values for the RMS DS was found to be about 9 and 5 ns for the 2–10 and 57–66 GHz bands, respectively. The Rician K-factor was found to be larger for the 60 GHz band, indicating that the ratio between the power in the direct path and the remaining scattered paths is larger at higher frequencies. In the paper, it is also argued that diffuse scattering plays a more important role in contributing to the overall received power in the 2–10 GHz band as compared to that at the 60 GHz band.

A comparison of the indoor propagation properties at 2.9 and 29 GHz was investigated in Koymen et al. [KPSL14]. Based on indoor measurement for two separate office floors, where one floor represents an office cubicle environment and the other floor represents office and hallway environments, estimated parameters for PL, excess delay, RMS DS and power profiles of the received paths are presented. The estimated PL parameters for the PL exponent and standard deviation of the log-normal shadowing distribution were found to be quite similar for the two bands. The RMS DS for 2.9 and 29 GHz was also evaluated, based on the measurements from each floor. In general, the RMS DS at 29 GHz is smaller. However, there were also occasions when the RMS DS was greater at 29 GHz, which the authors attribute to a better waveguide effect at 29 GHz in the hallways compared to at 2.9 GHz.

3.2.2 Characterisation of mm-Wave Radio Channels

3.2.2.1 Wideband characterisation
There are some contributions dealing with wideband characterisation at mm-wave frequency bands, including parameters such as PL and RMS DS. In Salous [Sal14], using a newly developed multi-band frequency-modulated continuous-wave (FMCW) channel sounder, 2×2 MIMO measurements where performed in an indoor environment typical of a large office working area. Results for the RMS DS give similar values for the four MIMO channels,

and show a significant increase as the threshold level is increased from 20 to 40 dB (0.42, 5.13, and 8.46 ns for the 20, 30, and 40 dB threshold levels, respectively). A PL exponent of 1.8 was also estimated from the measurements. In Barratt et al. [BNB15], an experimental measurement campaign using 60 GHz transceivers with on-chip antenna arrays is described. Measurement-based estimates of the PL exponents for a laboratory, office, corridor and an atrium environment were found to be 1.55, 1.55, 1.44, and 2.05, respectively.

The wireless mm-wave channel in a hospital environment, for real-time video streaming for angiography and ultrasonic imaging applications, was studied in Kyrö et al. [KHS$^+$12]. From the measurements, it was found that the shape of the power delay profile (PDP) was significantly different for the two scenarios, and seems attributed to the volume of the room and the degree of reverberation of radio waves in the room, as shown in Figure 3.7. The authors point out that PDPs with shapes similar to that of the ultrasonic inspection room also have been observed in an industrial environment where the reverberation of radio waves was significant due to the presence of a lot of metallic equipment in the environment. In the angiography room, the PDPs consist of a set of discrete specular components and the diffuse component having continuous power distribution.

In Haneda et al. [HJK$^+$14], measurement results for large indoor environments at 60 and 70 GHz are presented. Figure 3.8 shows two typical PDPs that were measured at 60 and 70 GHz. Specular paths accounted for at least 75% of the received power in the office scenarios and more than 90% in the shopping mall and station scenarios. The results suggest a possibility to use a single structural framework to model 60 and 70 GHz channels.

Finally, in Hafner et al. [HDM$^+$15], a fully polarimetric, wideband and directional radio channel sounding campaign conducted at 70 GHz is presented. In this contribution, propagation effects and characteristics that have to be considered in future Modelling were identified. It was found that more specular than diffuse components occur and that the channel is spatially sparse.

3.2.2.2 Spatial characterisation
In Martinez-Ingles et al. [MPR$^+$13], 10×10 MIMO measurements were performed at 60 GHz in an indoor laboratory environment at University of Cartagena, Spain. This laboratory consists of a room of dimensions $4.5 \times 7 \times 3$ m^3 and is furnished with several closets, desktops, and computers. Apart from wideband characterisation, the high-resolution parameter
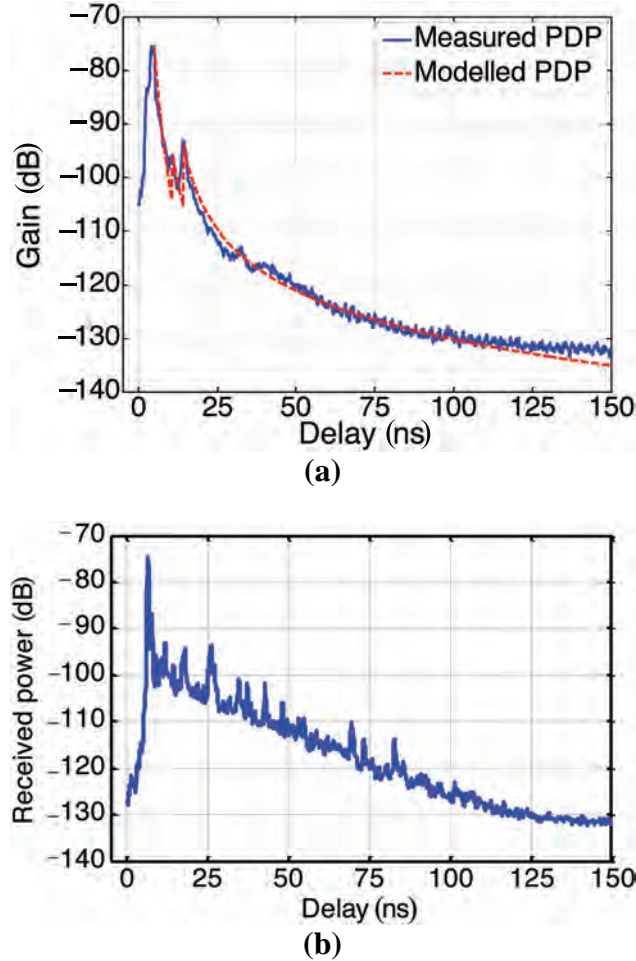
(a)

(b)

Figure 3.7 Typical PDPs of (a) the angiography room and (b) the ultrasonic inspection room [KHS+12].

estimator RiMAX was used to extract directional parameters, and compared to a 3D ray-tracing tool. The results show that the angular and DSs obtained from RiMAX are quite similar to the ones based on the 3D ray tracing tool.

Another contribution to angular characterisation can be found in Zhang et al. [ZYL+14], where channel measurement campaigns at centre frequency of 72 GHz with 2 GHz bandwidth were presented. The statistics of the composite and cluster-level spreads of channels in azimuth and elevation of
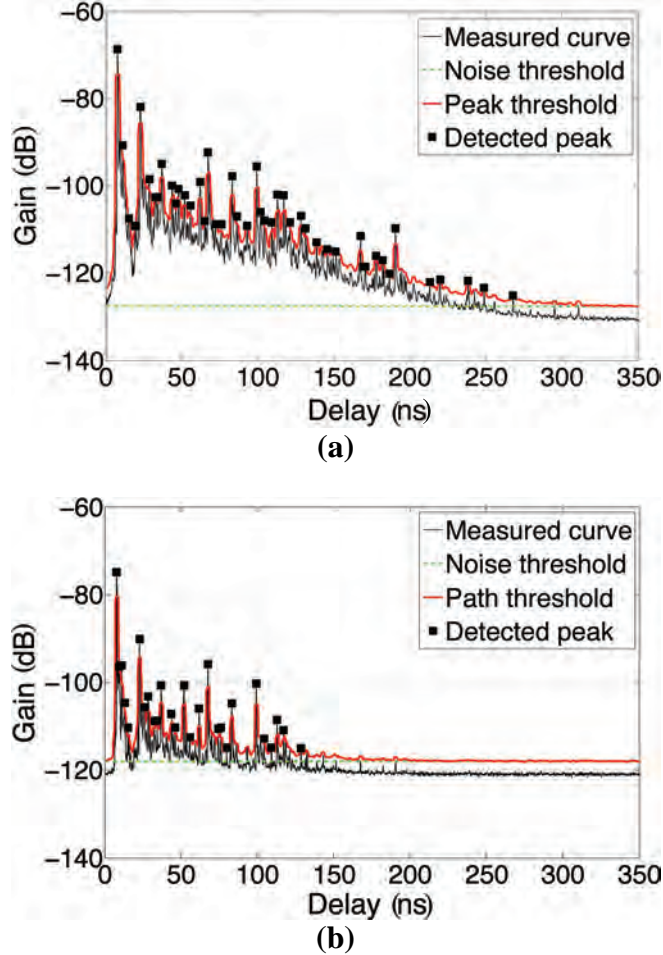
Figure 3.8   Exemplary PDPs in a large office: (a) 60 GHz and (b) 70 GHz. The PDPs were measured at the same Tx and Rx location [HJK+14].

arrival domains were calculated based on the angular power spectra. Less than four clusters can be identified in the direction of arrival domain. Laplacian distributions were found to fit well with the empirical occurrence of most of the angular-domain spread parameters considered. The estimated mean cluster azimuth spreads were found to be 6 and 9° for LoS and NLoS scenarios, respectively, and the mean cluster elevation spread is 6° in both cases.

In [Med15], 60 GHz measurement data based on an extreme size virtual antenna array ($25 \times 25 \times 25 = 15625$ elements), is used to provide highly
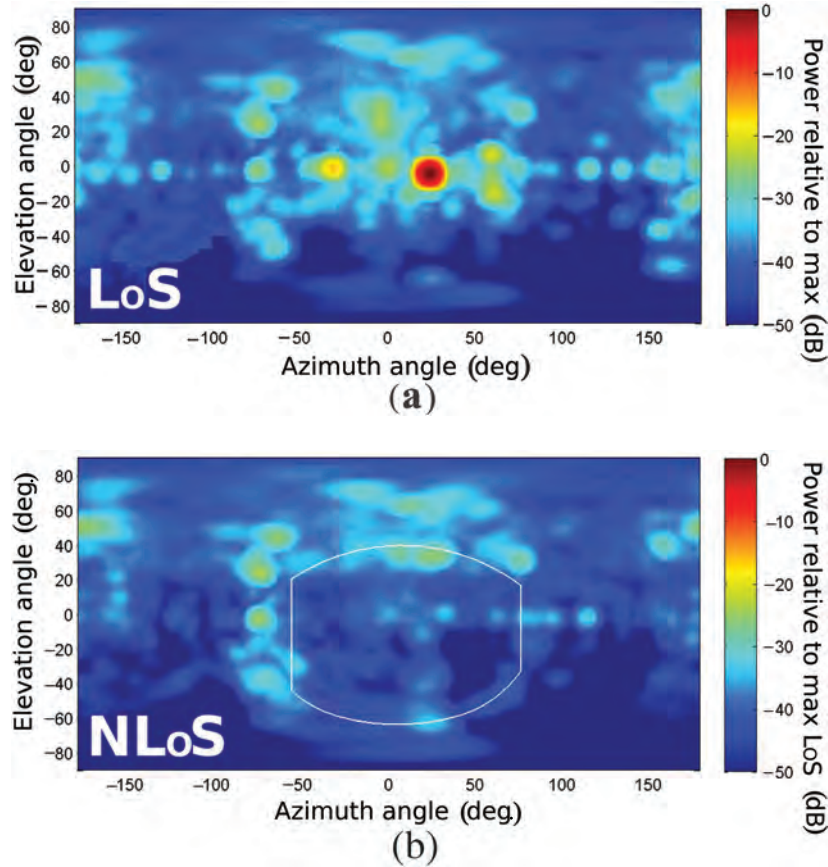
Figure 3.9 60 GHz directional power spectra for indoor line of sight (LoS) and non line of sight (NLoS) measurements. In the NLoS figure, the blockage by a white-board is indicated by a *white line*.

resolved directional properties of the radio propagation channel. The results indicated that the distinct spikes observed in the PDPs were caused mainly by specular reflections. There were however also a significant diffuse contribution due to scattering caused by the many smaller objects of the environment. Furthermore, corresponding LoS and NLoS channels were found to be very similar in directions where no blockage occurs, as seen in Figure 3.9.

3.2.2.3 Polarisation characterisation

The polarisation properties of mm-wave channels have been studied sparsely. In Dupleich et al. [DSF+14], quad-polarised 60 GHz channel measurements

have been carried out in a small-office environment. The identified strongest paths clearly indicate the need of using beamforming in NLoS scenarios. Furthermore, the presence of different paths with different polarisations shows the advantage of considering polarisation diversity in the beamformer.

A study of the cross-polarisation ratios (XPRs) of the propagation paths is presented in Karttunen et al. [KHJP15], based on measured indoor 70 GHz channels. Despite very extensive measurement campaigns with 23 channel sounding campaigns and 518 propagation paths detected in total, only 17 paths have detectable cross-polarisation power levels above the noise floor. A range of the XPRs between 10 and 30 dB is observed in Figure 3.10. Polarimetric radio channel measurements at 60 GHz in a small meeting room and in an empty, unfurnished conference room have also been presented in Gustafson and Tufvesson [GT15]. The results showed that the specular XPRs were in the range of 5–30 dB, which is consistent with the previous contribution. The XPRs can also be modeled as normally distributed random variables with a mean and standard deviation of 17.1 and 5.2 dB, respectively. Furthermore, in Degli-Esposti et al. [DEFV$^+$15], directional polarimetric 60 GHz indoor measurements were presented. These measurements were used to modify and calibrate a 3D ray-tracing model, and to tune the embedded effective-roughness diffuse scattering model.
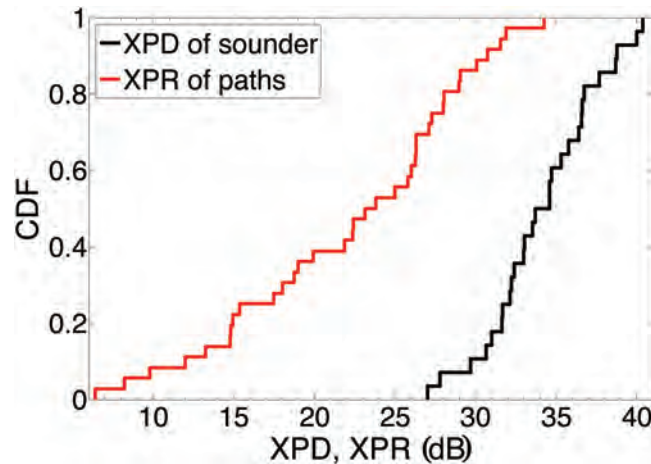

Figure 3.10 Cumulative distribution functions (CDFs) of the cross-polarisation discriminations (XPDs) and cross-polarisation power ratios (XPRs) for 70 GHz channels in large indoor environments [KHJP15].

3.2.3 Channels Models for mm-Wave Systems

Wireless channel modelling is always subject to a trade-off between the complexity and accuracy. Cluster-based, double-directional channel modelling is a popular compromise of the trade-off, as it supports wideband directional channel modelling, which is vital for beamforming, and can be used to derive a propagation channel model that is valid for arbitrary antenna elements and array configurations, while maintaining the complexity to a manageable extent.

3.2.3.1 Stochastic channel models

In Gustafson et al. [GHWT14], an indoor 60 GHz stochastic channel model was derived based on results from a measurement campaign in a conference room environment. The model is based on an extended Saleh–Valenzuela model, where the impulse response, h, is given by

$$h(t, \Theta_{\mathrm{rx}}, \Theta_{\mathrm{tx}}) = \sum_{l=0}^{L} \sum_{k=0}^{K_l} \beta_{k,l} e^{j\chi_{kl}} \delta(t - T_l - \tau_{k,l}) \delta(\Theta_{\mathrm{rx}} - \Omega_l - \omega_{k,l})$$
$$\delta(\Theta_{\mathrm{tx}} - \Psi_l - \psi_{k,l}). \tag{3.3}$$

Here, $\beta_{k,l}$ is the complex amplitude of the kth ray (i.e., MPC) in the lth cluster and T_l, Ω_l, and Ψ_l are the delay, direction of arrival (DOA) and direction of departure (DOD) of the lth cluster, respectively. Similarly $\tau_{k,l}$, $\omega_{k,l}$, and $\Psi_{k,l}$ are the delay, DOA and DOD of the kth ray in the lth cluster, respectively. Finally, $\delta(\cdot)$ is the Dirac delta function and the phase of each ray, $X_{k,l}$, is assumed to be described by statistically independent random variables uniformly distributed over $[0, 2\pi)$. The statistical properties of the inter-cluster parameters T_l, Ω_l, and Ψ_l, as well as the intra-cluster parameters $\tau_{k,l}$, $\omega_{k,l}$ and $\Psi_{k,l}$ were investigated. It was found that the ray and cluster fading were both appropriately modeled using a log-normal distribution, whereas the intra-cluster angles are modeled as Laplacian-distributed. The estimated channel model parameters can be found in Gustafson et al. [GHWT14].

In the work of Kyrö et al. [KHS+12], a different type of stochastic channel model was suggested for three different indoor hospital environments. This channel model does not include angular information, but is able to reproduce the typical shapes of the PDPs in the different environments. For the angiography room environment, a typical PDP consists of several narrow peaks and an exponentially decaying power distribution. These PDPs are

modeled as a set of specular components and a so-called diffuse part caused by distributed diffuse scattering:

$$\text{PDP}(\tau) = \sum_{n=1}^{N_s} P_n \delta(\tau - \tau_n) + P_{0\text{dif}} \exp\{-(\tau - \tau_0)/\beta\}. \qquad (3.4)$$

Here N_s is the number of identifiable specular components, P_n and τ_n is the power level and the excess delay of the nth specular component, respectively. $P_{0\text{dif}}$ and β is the initial power level and the decay constant of the diffuse component, respectively, and τ_0 is the delay of the first arriving component.

Unlike the angiography room, in the ultrasonic imaging room, a PDP consists of one or several clusters, which start from a distinguishable peak followed by a decaying tail of power. For this reason, the PDP for the ultrasonic inspection room is instead modeled using a power law model for the power of the nth cluster, as

$$P_n(\tau) = P_{n0}(\tau + \tau_{n0})^{-\alpha_n}, \quad \tau \geq \lambda_n, \qquad (3.5)$$

where P_{n0}, τ_{n0}, and α_n are the initial power value, offset delay, and decay constant for the nth cluster, respectively, and λ_n is the delay time from which the nth cluster begins. The modelling parameters, and the associated distributions, for the angiography and ultrasonic inspection room can be found in Kyrö et al. [KHS$^+$12].

3.2.3.2 Site-specific channel models

As it has been observed that the diffuse spectrum seems to be less significant for mm-wave channels compared to lower frequencies, and the major part of the received power in many mm-wave scenarios stem from specular reflections, it has been argued that ray tracing [MGG$^+$12] or other deterministic approaches [JHK$^+$12] might be viable at mm-wave frequencies. In Järveläinen et al. [JHK$^+$12], a site-specific model is presented, where the room dimensions of an ultrasonic inspection room have been measured with a laser scanner in order to produce an accurate, so-called point cloud model of the room. In the ray tracing simulations, each point in the point cloud generates one scattering component using a single-lobe directive scattering model. Results show that the model is able to predict the measured PDP reliably within a 20-dB dynamic range relative to the LoS component, using a single-bounce scattering assumption. Below this range, higher order interactions need to be considered, as evident from Figure 3.11.
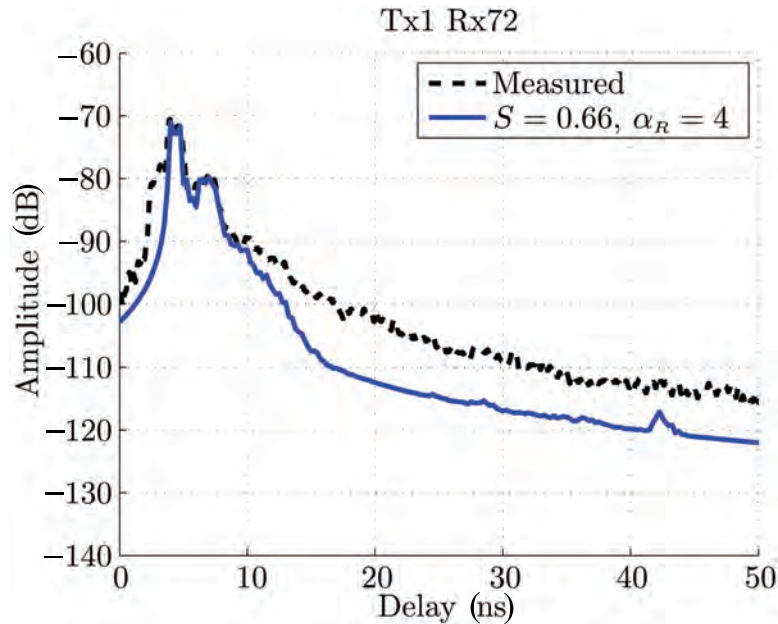
Figure 3.11   Comparison between measured and simulated PDP in a hospital room [HJK$^+$14].

In Martinez-Ingles et al. [MGG$^+$12], results from a measurement campaign in a laboratory environment is compared with the results from ray tracing simulations of the same environment. The 3D environment model in the ray tracing routine also includes important objects such closets, tables and windows, and appropriate values of the permittivity of different materials are assigned to different materials, based on values presented in the literature. By comparing the measured PDPs with the simulated ones based on ray tracing, it could be concluded that the ray tracing results agree fairly well with the measured PDPs in terms of the received powers and RMS DSs. However, when visually comparing the measured and simulated PDPs, it is clear that the ray tracing simulation is unable to predict some of the strong specular paths that are present in the measured PDPs.

3.2.3.3 Ray tracing and stochastic modelling

For mm-wave indoor channels, another popular approach is hybrid modelling with both deterministic and stochastic parts in combination. An example of this is the IEEE802.11ad channel model, where the inter-cluster angles are determined based on ray tracing and the gain of the LoS component is
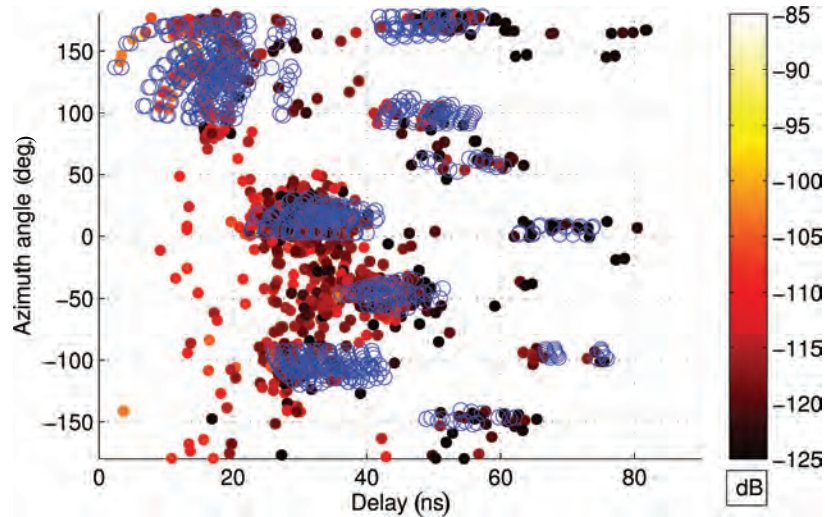
Figure 3.12 Delay and azimuth angles of estimated multi-path components (*dots*) and ray-tracing results for first, second and third order reflections (*circles*).

modeled using a deterministic expression. In Gustafson et al. [GHWT14], a purely stochastic channel model for a 60-GHz indoor scenario is compared with a hybrid channel model where the inter-cluster angles are determined using ray tracing, similar to the IEEE802.11ad model. The results in the paper show that both the stochastic and hybrid models offers a good agreement with the measured channels. In Figure 3.12, the delay and azimuth angles of the MPCs estimated with the high-resolution SAGE algorithm are compared with the estimated delays and angles from the ray tracing simulation, for all the measured scenarios in Gustafson et al. [GHWT14]. Similar results were obtained for the elevation angles. As seen in the figure, there is a there is a considerable overall agreement, but there are also many multi-path components with significant power that are not explained by the ray tracing simulations. This is a direct result of an over-simplified environment model in the ray tracing routine, indicating the fact that it is necessary to include finer structures in the model for the room environment.

3.2.4 Capacity Evaluation of mm-Wave Systems

3.2.4.1 OFDM and single carrier (SC)

Implementation of IEEE physical layer (PHY), such as IEEE802.15.3c and IEEE 802.11ad, have been one of the investigation areas in COST IC-1004.

The orthogonal frequency division multiplexing (OFDM) or SC specifications have been used in Takizawa et al. [TKH$^+$12]. The evaluation of 60 GHz high-speed radio systems has been conducted through calculation of SIR, channel capacities, and achievable TPs by using measured PDPs in hospital environments. The results reveal that OFDM systems provide the required TP for the application scenario in all the measured PDPs. On the other hand, the SC systems without any equalisation are limited to 75% of the measured PDPs where the required TP is achieved. Figure 3.13 shows the TPs for OFDM and SC using both standards.

Extending this approach to MIMO, in Martinez-Ingles et al. [MSM$^+$13], the performance of IEEE 802.15.3c MIMO–OFDM systems for four antenna configurations has been experimentally studied. The correlation was highly influenced by the antenna configurations, since the arrangement of the antenna has a large impact on the performance, especially over short distances. In addition, MIMO seems a reasonable solution for both increasing the TP and the communication distance, as it was shown that a 4×4 QSTBC-MIMO system could increase the data bit rate by a factor of 3.7 and also increase the maximum achievable distance by 1 m.

3.2.4.2 Spatial multiplexing

The potential of spatial multiplexing at mm-wave frequency band is analysed in Haneda et al. [HKGW13]. The paper provides a measurement-based investigation of the spatial degrees-of-freedom (SDoF) of 60 GHz indoor channels. The SDoF are defined in a way so that they only depend on the propagation conditions and the sizes of the Tx and Rx antenna apertures. This way, the SDoF provides an upper bound on the number of eigenchannels that can be realised with a given antenna aperture size under the given propagation conditions. For an antenna aperture size of 9 λ^2 at 60 GHz, as seen in Figure 3.14, the SDoF is more than one for a Tx–Rx antenna separation of more than 2 m. Furthermore, at most ten antennas on each side of the Tx and Rx are sufficient to perform effective spatial multiplexing in the considered propagation scenario. Even five antennas can work efficiently to capture eigenchannels down to –15 dB relative magnitude.

3.2.4.3 Beamforming

At mm-wave frequencies, physically small antenna apertures can be electrically large. Therefore, mm-wave radios are inherently much more capable of focusing beams and obtaining large array gains than microwave radios. In Haneda et al. [HGW13], the authors compare the capacity improvement
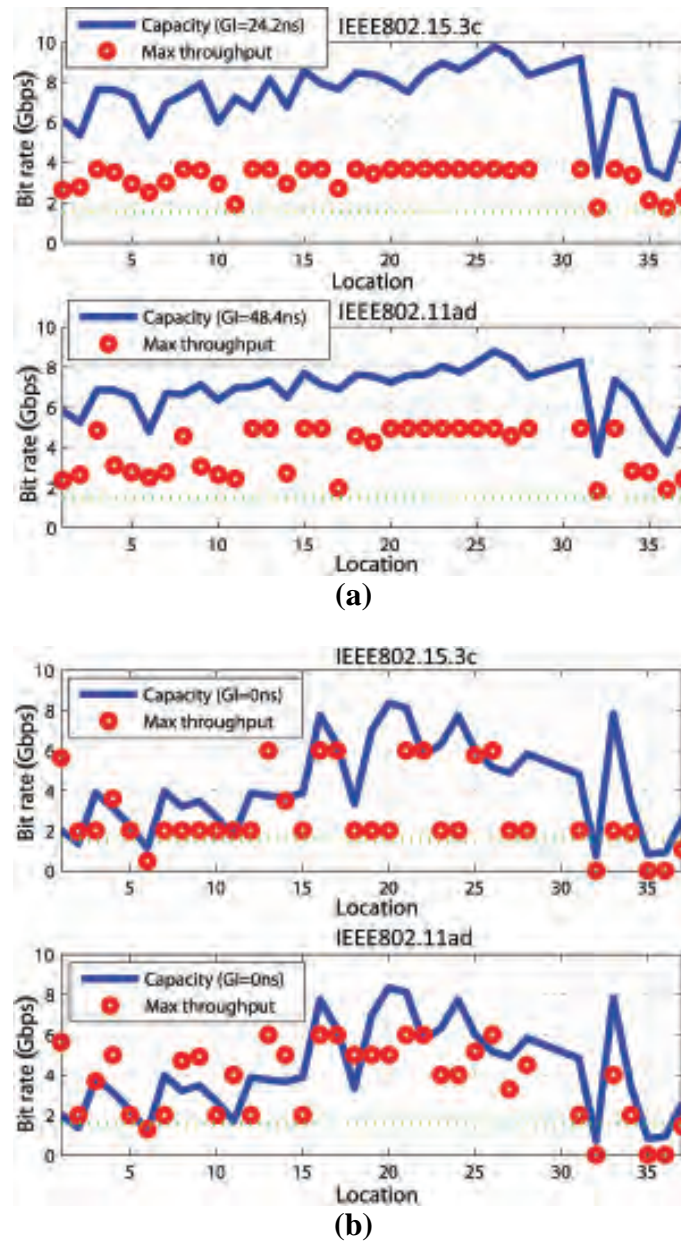
(a)

(b)

Figure 3.13 A comparison between the TPs (simulation results) and channel capacities calculated from measured PDPs (dotted lines show required TP of 1.53 Gbps); (a) Orthogonal frequency division multiplexing (OFDM), and (b) Single carrier (SC) [TKH+12].
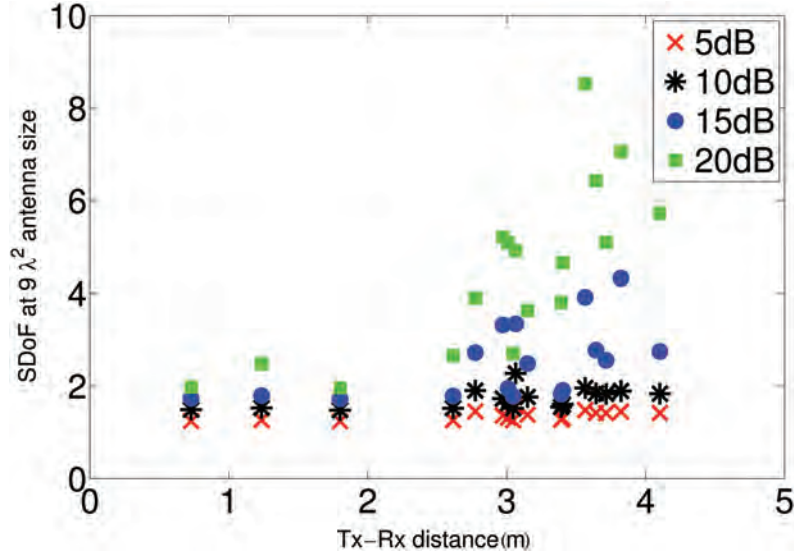
Figure 3.14 Distance dependency of the spatial degrees-of-freedom (SDoF) for an antenna aperture size of $9 \lambda^2$. The SDoF is plotted for different threshold levels, i.e., $t = 5, 10, 15$, and 20 dB [HKGW13].

capability of spatial multiplexing and beamforming techniques for 60 GHz spatial transmissions in a multi-carrier radio system, as shown in Figure 3.15. It is concluded that beamforming is, in general, as robust as spatial multiplexing in providing capacity enhancement in the 60 GHz band. Spatial multiplexing would be a worthwhile option when the Rx SNR is favorable and a higher peak data rate is required. A hybrid approach of beamforming and spatial multiplexing can be a sound compromise to take advantage of both techniques.

3.3 Techniques and Models for Localisation

Location awareness is a key component of many future wireless applications and a key enabler for next-generation wireless systems. The core challenge is achieving the required level of localisation accuracy *robustly,* especially in indoor environments which are characterised by harsh multipath conditions. Promising candidate systems thus either provide remedies against multipath or they fuse information from complementary sensing technologies [SMW12, CDG+14].

This section starts with the modelling and characterisation of "deterministic" channel properties that are relevant for positioning (Section 3.3.1).
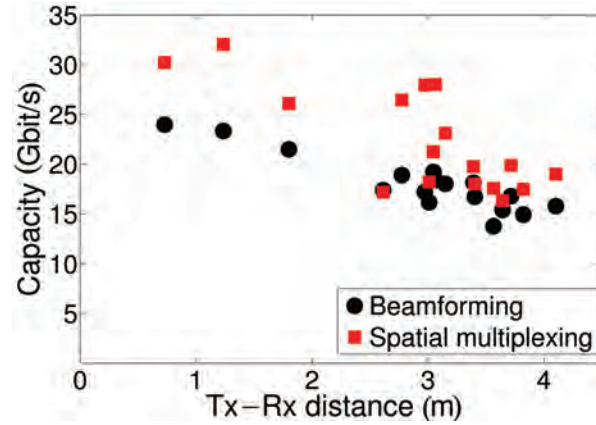
(a)
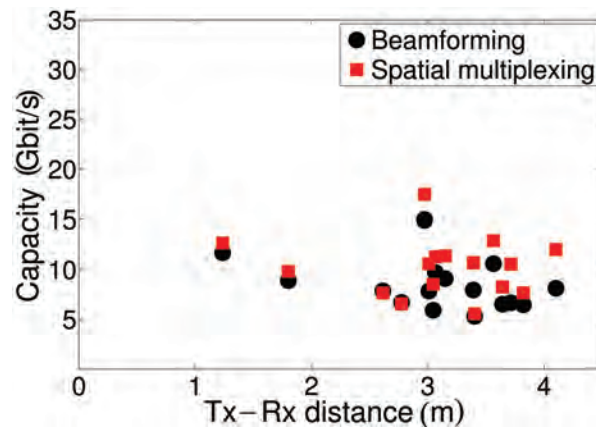
(b)

Figure 3.15 Comparison of the ergodic channel capacity for beamforming and spatial multiplexing. (a) 9 λ^2 antenna aperture size, and (b) NLoS scenario with antenna aperture size of 9 λ^2 [HGW13].

The acquisition of position measurements from received signal is then discussed in Section 3.3.2. Different system architectures that can be used for indoor positioning are addressed in Section 3.3.3, while Section 3.3.4 summarises algorithms that *exploit* position-related information from the multipath channel beyond the LoS component, as suggested by the discussion in Section 3.3.1.

3.3.1 Radio Channel Characterisation for Positioning

Geometric information related to the position of the agent (the radio device to be localised) is found not only in the LoS component, but also in "deterministic" reflected MPCs. This motivates to exploit such components for positioning and also to model such components in a geometrically consistent way. The analysis of performance bounds quantifies the amount of information obtained from these components.

3.3.1.1 Performance bounds motivating channel modelling

In Witrisal and Meissner [WM12], the (baseband) signal received at an agent has been described as

$$r(t) = \sum_{k=1}^{K} \alpha_k s(t - \tau_k) + s(t) * v(t) + w(t), \qquad (3.6)$$

where, $s(t)$ is a signal that is transmitted from/to an anchor, a reference node at known location $\mathbf{p_1}$. The *deterministic* part of the channel is given by the sum over K MPCs, scaled and shifted by the complex amplitudes α_k and delays τ_k, respectively. The delays $\tau_k = \frac{1}{c} \|\mathbf{p} - \mathbf{p}_k\|$ are deterministically related to the positions $\mathbf{p}$ of the agent and $\mathbf{p}_k$ of virtual anchor (VA) that describe the geometry of the propagation paths [WM12]. The signal $v(t)$ denotes diffuse multipath, i.e., everything that is not or can not be modeled by the deterministic part. It is modeled as a (Gaussian) random process with auto-covariance $\mathrm{E}\{v(\mathrm{t})v^*(\tau)\} = S_\mathrm{v}(\tau)\delta(t - \tau)$, where $S_\mathrm{v}(\tau)$ is a PDP accounting for the non-stationary variance of the diffuse multipath in the delay domain. Finally, $w(\mathrm{t})$ is Gaussian measurement noise at power spectral density (PSD) N_0.

Using this model, the Cramér Rao lower bound (CRLB) on the position error can be derived. The Fisher information matrix is the inverse of the CRLB, which quantifies the information about the position $\mathbf{p}$ contained in the received signal $r(t)$. Under the assumption of *separable* deterministic MPCs, it is written as

$$\mathbf{J_p} = \frac{8\pi^2\beta^2}{c^2} \sum_{k=1}^{K} \mathrm{SINR}_k \mathbf{J}_r(\phi_k), \qquad (3.7)$$

where, β denotes the effective (RMS) bandwidth of $s(t)$ and c is the speed of light. Furthermore, $\mathbf{J}_\mathrm{r}(\phi_\mathrm{k})$ is a unitary rank-one matrix with an eigenvector pointing along the angle-of-arrival (AoA) of the k-th MPC, the line connecting $\mathbf{p}$ and $\mathbf{p}_k$. According to this equation, each MPC adds position-related

information. The *amount* of this information is quantified by the signal to interference plus noise ratio (SINR) of the respective MPC, which is defined as [WM12]

$$\text{SINR}_k = \frac{|\alpha_k|^2}{N_0 + T_\text{p} S_\text{v}(\tau_k)}. \tag{3.8}$$

It evaluates the ratio of the MPC's energy $|\alpha_k|^2$ to the noise density N_0 and the interference term $T_\text{p} S_\text{v}(\tau_\text{k})$. The latter is quantified by the product of the PDP $S_\text{v}(\tau)$ of the diffuse multipath and the pulse duration T_p, the bandwidth inverse of $s(t)$. Equations (3.7) and (3.8) quantify the contributions of individual deterministic MPCs to the position information available from the received signal $r(t)$. This result clearly highlights the beneficial influence of a large bandwidth through β and T_p [WML$^+$14].

3.3.1.2 Channel analysis

In Meissner and Witrisal [MW12], an estimation technique has been proposed for the SINRs Equation (3.8) to evaluate the available position-related information from real measurement data. The method works with signals captured at known locations in the environment. Figure 3.16 shows a few such signals and the SINR estimates. MPCs with stable amplitude tracks have large SINRs, indicating high reliability of their position information. These reflections are less impaired by interference through diffuse multipath.

The figure also shows the energy capture (EC) of these MPCs, the relative amount of energy they carry. A method to extract this parameter is discussed in Meissner et al. [MAGW11]. These numbers show that about 70% of the energy can be attributed to geometrically modeled MPCs. The LoS component already carries almost 50%. Clearly, a large fraction of energy originates from the deterministic components. However, energy does not directly translate into position-related information, as seen from a comparison of the SINR and EC values in Figure 3.16.

3.3.1.3 Channel modelling

The evaluation of the *robustness* of a localisation system requires extensive experimental campaigns that span a sufficient range of target environments. These are, however, tedious to perform. Alternatively, geometrically consistent channel models may be used to generate *synthetic* signals in test environments; a possible way forward to facilitate a robustness analysis [JHK$^+$11]. The degree of realism can be evaluated based on (i) the position-related signal
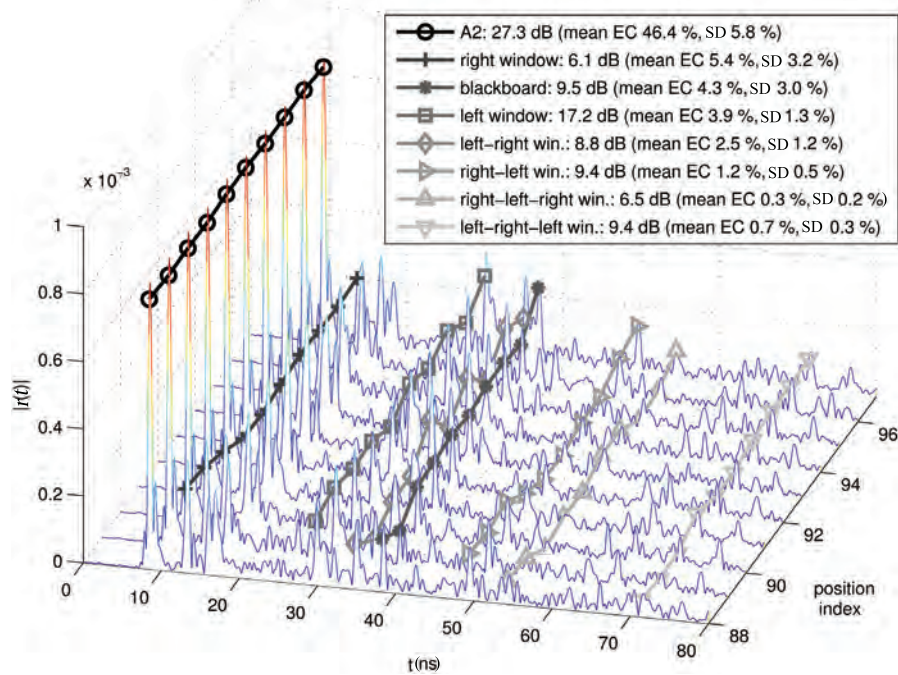
Figure 3.16 Signals obtained at closely spaced locations (5 cm spacing) in a seminar room [MLLW13]. Estimated amplitudes of geometrically modelled MPCs are indicated, together with their estimated signal to interference plus noise ratio (SINR) and energy capture (EC).

parameters (time-of-arrival (TOA), AOA, receive-signal-strength (RSS), etc.) and (ii) also in the light of position information, as defined by Equation (3.8). In the latter, also the level of diffuse multipath is accounted for. It is paramount to consider LoS, NLoS and OLoS situations, since the LoS component is generally considered to carry most of the position-related information [JHK^{+}11]. All these effects are related to the geometry of the environment.

A useful channel model for the performance analysis of indoor localisation systems will thus be a geometry-based stochastic channel model (GSCM), in which the stochastic part needs to account for the geometrically non-resolvable components of the channel. The deterministic part needs to be spatially consistent and the overall model should be parametrised by measurements. Also, factors such as the mobility of the agents on a sufficiently large scale and cooperative multilink schemes must be supported to reflect the needs of future applications [AMAU14].

Ray-tracing is a deterministic and geometric technique that is by default suitable to syntesise geometrically consistent CIRs. However, a realistic consideration of diffuse multipath is often difficult and computationally intensive. To tackle this, surfaces are typically subdivided in tiles whose size depends on the wavelength and scattering lobes are used for each tile to create a number of weighted outgoing scattered rays [DEFV+07, GXH+15, MGM+13]. As Figure 3.17(a) shows, this can model the diffuse multipath for small excess delays reasonably well. But for larger delays, the power level drops significantly below the measured reference. A promising alternative is the combination with stochastic propagation graphs [SPG+14]. A graph structure is used to model recursive interactions between scatterers that may be placed according to stochastic or geometric considerations. A closed-form solution can be given for the channel transfer function, allowing for realistic levels of diffuse multipath as illustrated in Figure 3.17(b).

3.3.2 Estimation of Position-Related Parameters

The estimation of position-related parameters (position measurements) is usually the first step towards localisation and tracking. That is, parameters such as the TOAs, time-difference-of-arrival (TDOAs), AOAs, or RSSs are extracted from the received signals. These parameters are related to the geometry at hand through known or learned functional models.

This subsection summarises approaches towards the estimation of these parameters. We first discuss papers that deal with the estimation of the TOA and AOA of the received signal or its components. We then put our focus on the important problem of detection and mitigation of NLoS conditions.

3.3.2.1 Ranging in multipath channels and multipath parameter estimation

A conventional estimator of the TOA estimates the CIR from the received signal from which then the leading edge can be extracted. This approach is particularly problematic when separability conditions are violated, e.g., at non-UWB bandwidths. Furthermore, popular algorithms like estimation of signal parameters via rotational invariance techniques (ESPRIT) and SAGE require knowledge of the number of MPCs.

An approach that avoids these complications is discussed in Jing et al. [JPF14]. A stochastic point-process model of the channel is used to obtain a *direct* estimation of the TOA from the received signal. A ML estimator has been formlated and evaluated for LoS and NLoS conditions. Simulation results
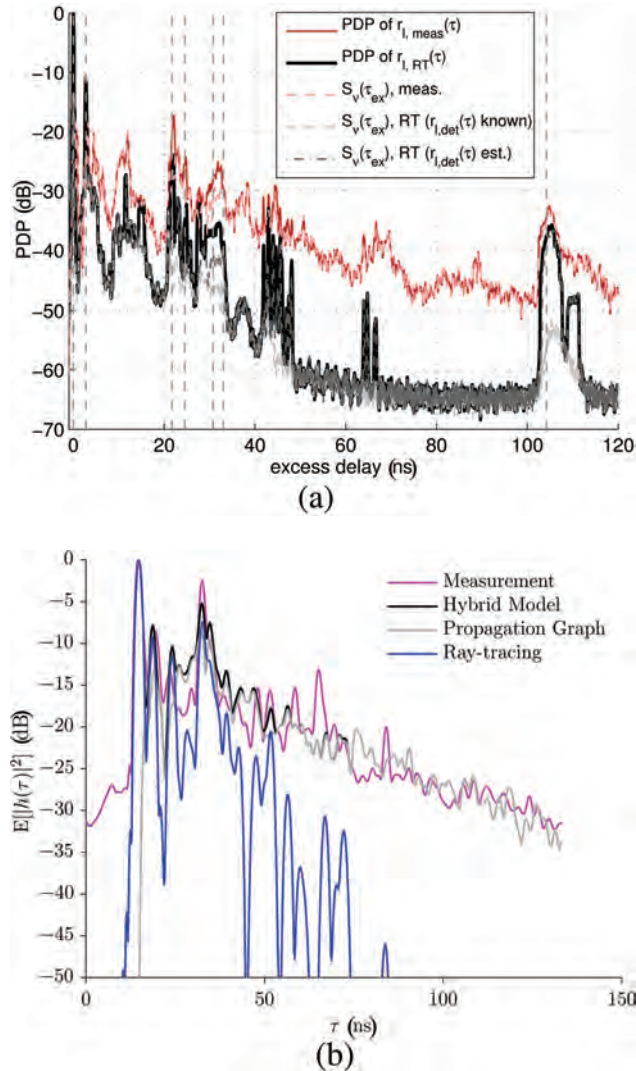
Figure 3.17 Channel modelling concepts developed within COST IC1004: (a) Ultra wideband (UWB) Ray-tracing [GXH+15] accounting for diffuse multipath compared to measurements [MGM+13], and (b) modelling of deterministic and diffuse multipath with a stochastic propagation graph combined with ray-tracing [SPG+14].

show the superior performance over conventional estimators. An OFDM signal with a bandwidth of about 7.5 MHz has been used. The impact of model mismatches is rather small if an NLoS scenario is assumed.

Section 3.3.1 has introduced an approach to quantify the position-related information contained in deterministic MPCs by their SINR values. This discussion highlighted the importance of a stochastic characterisation of diffuse multipath that interferes with useful components.

The same basic finding has been reported in Tanghe et al. [TGJ+12], which compares the performance of classical multipath estimation algorithms, namely SAGE and ESPRIT, to the more recent RiMAX algorithm. Only the latter accounts for the presence of dense multipath and hence outperforms the others, as shown in Figure 3.18. The results are based on synthetic data that are generated by a ray-tracing algorithm. A parametric model is used in the estimator for the dense mulipath, consisting of an exponentially decaying PDP. Four-by-four-antenna arrays are used at TX and RX, the data have a bandwidth of 40 MHz, and the estimated parameters include AoA, angle of departure (AoD), and TOA. A related positioning approach has been discussed in Zhu et al. [ZVK+15].

For high-accuracy indoor localisation, MPCs can be extracted from UWB channel measurements [MLLW14, MLW14, LMLW15]. Assuming that the
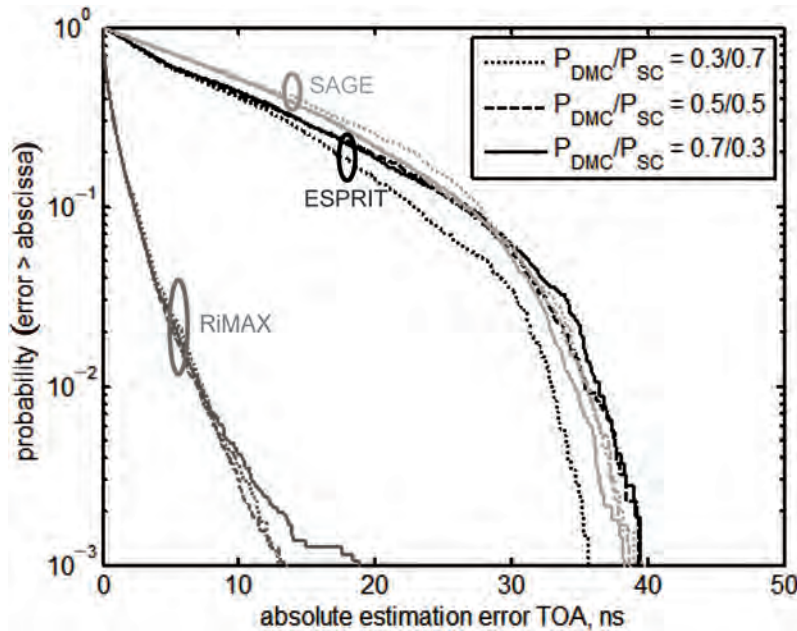

Figure 3.18 Complementary cumulative distribution functions (CCDFs) of absolute time-of-arrival (TOA) estimation error for different power ratios of deterministic to diffuse multi-path components (DMCs) [TGJ+12].

large bandwidth can provide separability of MPCs in the delay time, a relatively simple, iterative, correlation-based estimator can be used in a first step to estimate the TOAs. For example, the arrival time estimation for the k-th MPC is realised as an iterative least-squares approximation of the received signal $r(t)$

$$\hat{\tau}_k = \arg\min_\tau \int_0^T |r(t) - \hat{r}_{k-1}(t) - \hat{\alpha}(\tau)s(t - \tau)|^2 \, dt \qquad (3.9)$$

using a template signal $\hat{r}_{k-1}(t) = \sum_{k'=1}^{k-1} \hat{\alpha}_{k'} s(t - \hat{\tau}_{k'})$ for all MPCs up to the $(k-1)$-st. The path amplitudes are nuisance parameters, estimated using a projection of $r(t)$ onto a unit energy TX waveform $s(t)$ as

$$\hat{\alpha}(\tau) = \int_0^T [r(t)]^* s(t - \tau) dt; \hat{\alpha}_k = \hat{\alpha}(\hat{\tau}_k). \qquad (3.10)$$

The work in [MLLW14, MLW14, LMLW15] is based on this approach. It accounts for diffuse multipath only in the second step, the positioning/tracking algorithm. This is achieved by weighting the different MPCs based on their position-related information that is quantified by their SINRs (cf. Section 3.3.1).

In Froehle et al. [FMW12], a probability hypothesis density (PHD) filter is used for simultaneous tracking of several MPCs in UWB measurements. The PHD filter is a multi-target tracking algorithm that can cope with varying path visibility and an unknown number of paths. It uses input data extracted from UWB measurements (6–8 GHz) as described in Equations (3.9) and (3.10).

3.3.2.2 NLoS detection and mitigation

Non-line of sight conditions have particularly adverse impact on indoor localisation. In indoor environments, due to large number of walls, obstacles, and moving people, the first arrival path between a transmitter and a receiver is rarely LoS. Consequently, each localisation-aimed measurement, i.e., TOA, TDOA, AOA, or RSS will be significantly biased, leading to an erroneously estimated position.

As the NLoS effect is one of the main sources of localisation errors, a wide range of NLoS identification and mitigation techniques has been already proposed. A thorough survey of such techniques can be found in Kulakowski [Kul12]. The first common approach is to distinguish between LoS and NLoS anchors, i.e., to identify which anchors have a clear LoS to the localised object. If there is a redundancy in the number of anchors available, the object

position can be estimated for each subset of anchors independently, and then the credibility of each estimation is calculated on the basis of residual errors resulting from the position estimation [Che99]. The second solution is to use advanced statistics of the received signal. Parameters like the kurtosis, maximum excess delay, and RMS DS can be efficiently exploited in order to decide if the path to an anchor is of LoS or NLoS type. In residential, urban and indoor office environments, the mean kurtosis is lower, while the maximum excess delay and RMS DS are higher in NLoS than in LoS channels. An example where the received signal statistics are used is the research work presented in Cipov et al. [CDP12]: the LoS and NLoS propagation conditions are distinguished calculating kurtosis. In Jing et al. [JPF14], which is also discussed in the previous subsection, a statistical TOA estimation method is proposed that is inherently robust against NLoS situations.

Another option is a cooperative approach: if the anchor signals are not sufficient for a node to determine its position, the network nodes can cooperate exchanging some data between each other. Wireless nodes perform ranging measurements and exchange the position estimates with their neighbours. Then, each node calculates its own position again, using the data from neighbouring nodes [SRL02].

When dealing with NLoS issues, fingerprinting techniques are also an interesting option [KK04]. They are very well suited to work without direct LoS visibility between the localised object and the anchors, because their basic idea is just to match data patterns (to look for their similarities) independently of the scenario these patterns describe in reality. However, gathering training data is troublesome and frequently not feasible. Moreover, it means the localisation system is not robust to environment or network topology changes.

A wide group of solutions is related to UWB systems. UWB systems are working in extremely large frequency bandwidth, which makes them potentially very accurate, but still susceptible to NLoS situations. The ability to distinguish MPCs at a UWB receiver opens the door for positioning techniques that can even take advantage of the multipath propagation phenomenon [GE11]. In combination with tracking filters, reflected MPCs can be utilised to retain robust localisation when the LoS signal gets obstructed.

3.3.3 Localisation and Tracking Systems

3.3.3.1 RSS-based systems

While in outdoor environments the satellite-based systems are a widely accepted standard, in indoor scenarios (where satellite signals do not penetrate

walls) wireless localisation remains an open issue. Among other solutions, RSS techniques are gaining significant attention, mainly due to their simplicity and the ability of collecting data from the wide variety of heterogeneous wireless devices. These techniques, however, usually suffer from a lack of accuracy resulting from multipath propagation.

The issue of reliability of RSS-based systems is addressed in [KRG$^+$14]. The results of a measurement campaign in a large single-floor laboratory show that the classical multilateration scheme does not perform well in such an environment: multipath propagation and shadowing effects are the reasons for very strong variations in the received signal levels and there is no clear dependence between the distance and the PL (Figure 3.19). On the other hand, a localisation algorithm based on calculating the weighted mean of the anchor positions (where the weighting coefficients are proportional to the signal power levels received from the anchors) results in much better accuracy, comparable with other indoor localisation schemes reported in literature. The weighting mean algorithm copes well with shadowing (NLoS) effects: if an anchor receives a reflected signal instead of a direct one, the weighted coefficient for this anchor is smaller. It weakens the impact of this anchor in final calculations, but it does not corrupt them, like in the case of multi-lateration. Using the frequency diversity also seems to be a promising solution: the authors report that it reduces the localisation error by about 30%.

These measurements are later continued with a mobile node to be localised (tracked) [KRO13]. With the weighted mean algorithm and Kalman filtering, a localisation accuracy of 2–2.5 m can be obtained.

An interesting solution is also proposed in Redzic et al. [RBO12]. A hybrid system based on camera images and RSS data from wireless local area network (WLAN) access points is described. The image data from the cameras and the RSS data from WLANs are used separately to calculate the position of the user. Later, the localisation results are analysed together taking into account their confidence levels, which significantly improves the system accuracy.

3.3.3.2 Passive localisation

A passive localisation system registers and analyses the impulse responses of the radio channels between a fixed transmitter and UWB receivers installed in an indoor area. When a new object or a person appears, some of the propagation paths are blocked and the modified set of impulse responses is again registered in the system. Evaluating the changes in the radio environment, the system can estimate the object position [PW10a]. Passive localisation has a few important
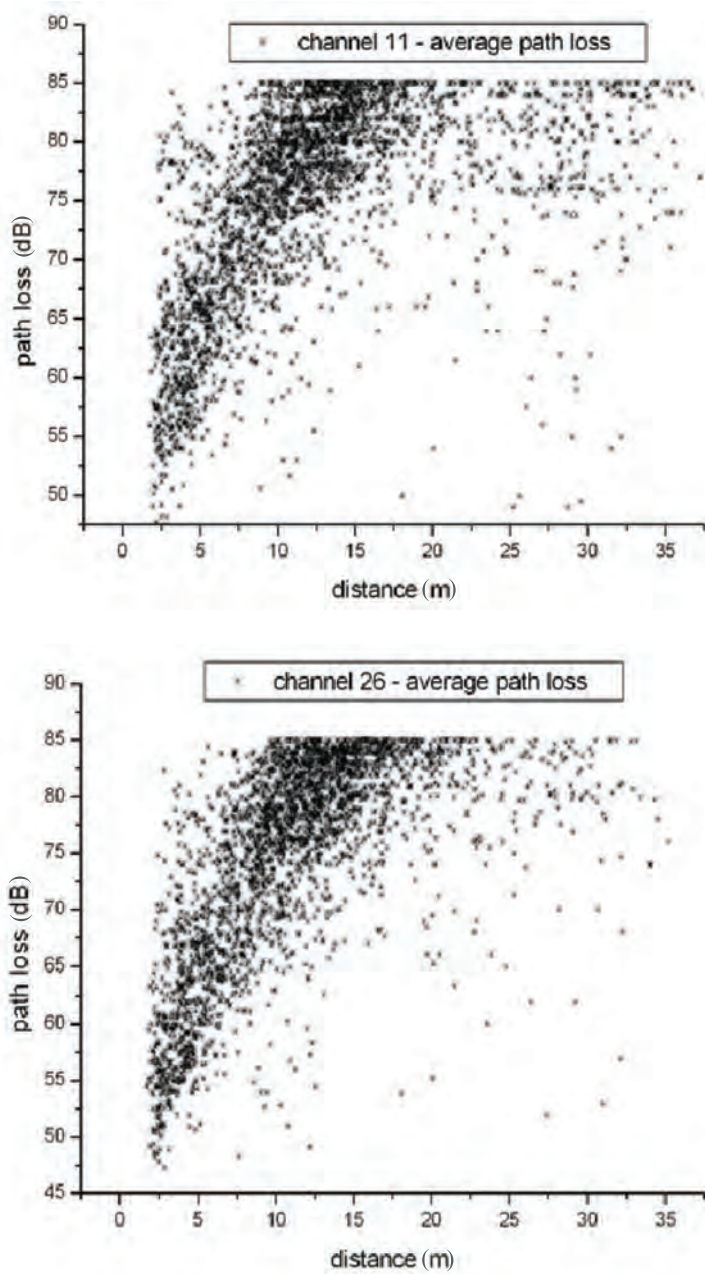
Figure 3.19   The PL as a function of the sensor–anchor distance for the channel 11 (2405 MHz) and the channel 26 (2480 MHz) [KRG+14].

merits that could decide about its future commercial success: (i) it can be used indoor, (ii) it does not need LoS visibility between a localised object and the system elements, and finally (iii) the localised object does not need to have any wireless device attached.

An example of a passive indoor UWB localisation system is analysed in Kosciow and Kulakowski [KK12] by means of computer ray tracing calculations. Two algorithms are used for calculating the object position. In the first one, an area where all the blocked propagation paths are crossing each other is considered as a possible position of the object to be localised. In the second approach, the sets of impulse responses resulting from all possible object positions (with a certain resolution) are analysed and juxtaposed with the set for the real object position. This research is continued in Kmiecik and Kulakowski [KK14], where not only localisation, but also simultaneous tracking of two objects is considered. This is later validated experimentally in Kmiecik et al. [KML$^+$15]. The aim is to detect the presence and to track the motion of a cardboard box with radio frequency absorbers on its surface, moving in a seminar room. With three transmitters and four receivers (12 fixed radio channels), localisation accuracy is quite satisfactory.

A related scenario is also investigated in Jovanoska et al. [JZG$^+$14], where measurements on a passive localisation system capable to work from beyond the wall are presented. The system is clearly motivated by radar solutions and is based on the signals reflected from the tracked people. The system consisting of a single transmitter and two receivers is able to track only one person; in order to track more people simultaneously the system should have more transceivers. The analysed system architecture has interesting security or military applications: a room under investigation can be inspected before entering it.

3.3.3.3 Radio-frequency identification (RFID) positioning on backscatter channels

Passive RFID is a technology used for the identification of tagged items. Significant effort has been spent on realising *positioning* methods for this technology, as this would bring added value to many applications. However, low-signal bandwidth and low-return power are two system properties rendering this capability extremely hard to realise. Multistatic (MIMO) readers and increased bandwidth are possible concepts towards the development of practical RFID positioning systems.

In Mhanna and Sibille [MS14], an experimental evaluation is shown of the power gain over the backscatter channel, when bistatic antenna setups and

UWB signals are employed. UWB signals would in principle allow for cm-level accuracy. A multistatic system with four reader transceivers (employing 16 channel branches) provides a mean gain of about 14 dB compared to a single monostatic reader. The gain over four monostatic readers is about 6.5 dB.

An appealing feature of an RFID system lies in the fact that the transponders sample the radio channel at defined locations. This fact may be used in a *cognitive* RFID positioning system [KLMA13] which learns the properties of the radio environment from past measurements in order to improve the efficiency of position measurements. The paper proposes a time-reversal processing for the transmitter side to focus transmit energy onto the tag. The analysis of the CRLB [LMFW14] demonstrates the impact of the transmitter-side processing on the information obtained from position measurements. This is an important property of a cognitive system that implements a perception–action cycle at the sensor level [HXS12].

3.3.4 Multipath-based Localisation and Tracking

In multipath-based localisation and tracking, MPCs can be associated to the local geometry using a known floor plan [MLFW13, MLLW14]. MPCs can simply be seen as signals from Vas/VSs. In particular in NLoS situations, a multipath-based method can increase the robustness of the localisation system tremendously. Competing approaches, discussed in Section 3.3.3, either detect and avoid NLoS measurements [MGWW10], mitigate errors induced by strong multipath conditions [WMGW12], or employ more realistic statistical models for the distribution of the range estimates [LMW13].

UWB signals are useful to separate MPCs because of their superior time resolution. Additional position-related information is thereby exploited that is contained in the multipath radio signals [MLW15] (cf. Section 3.3.1). Several contributions have been presented with in the COST action, which relate to this approach.

3.3.4.1 UWB techniques

The work in Meissner et al. [MLFW13] presents a comparison between multipath-assisted indoor localisation/tracking and conventional localisation/tracking methods that are based on TOA measurements. The former show superior performance in harsh indoor environments and NLoS situations. The presented algorithm uses the extracted multipath delays Equation (3.9) and the according position-related information introduced in Section 3.3.1 to properly weight the measurements. The estimated delays are associated to

the VAs using an optimal sub-pattern assignment algorithm. These VAs are then used as additional anchors for the tracking filter. An extended kalman filter (EKF) employs the position-related information as a measurement noise model, quantified in terms of the SINRs of the MPCs, Equation (3.8).

Figure 3.20 shows an example of the multipath-based tracking of an agent position using the EKF with data association (EKF-DA). Here only one anchor was used. The SINRs were estimated at 60 measurement positions indicated by
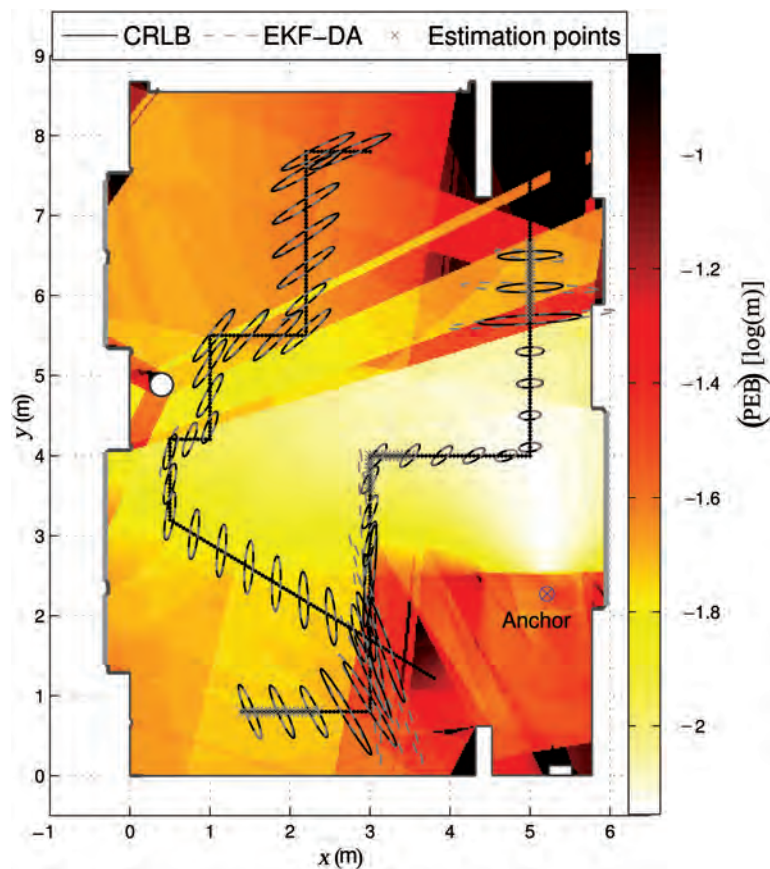

Figure 3.20 Position error bound (PEB) and tracking results for $T_{\mathrm{p}} = 0.5$ ns, $f_{\mathrm{c}} = 7$ GHz, and a single fixed anchor. The PEB Equation (3.7) has been computed from estimated SINRs Equation (3.8); *grey crosses* are the 60 estimation points for the SINRs. *Solid* and *dashed ellipses* denote the Cramér Rao lower bound (CRLB) and error covariance of the extended Kalman filter (EKF), respectively, at several points along the trajectories. All ellipses are enlarged by a factor of 20 for better visibility.

grey crosses. Also the position error bound (PEB) is shown over the entire floor plan. It has been computed using the estimated SINRs, providing a prediction of the spatial distribution of the achievable performance. We consider these maps as an indicator for the robustness of the localisation system.

A real-time implementation of this multipath-assisted tracking method has been described in [MLLW14] to demonstrate the practicality of this approach. This work presents an in-depth analysis of position-related information estimation and agent tracking for different environments. Therein, the estimated SINRs of the most dominant MPCs are analysed for two sample rooms and for centre frequencies of $f_c = 7$ GHz and $f_c = 8$ GHz. The performance of the EKF is analysed, evaluating the impact of the prior knowledge of the SINRs. A significant gain results from this additional model knowledge. In Meissner et al. [MLW15] it has been shown that the SINRs can be learned online during the tracking of the agent.

In contrast to this *tracking* technique, a multipath-assisted indoor *positioning* algorithm has been presented in Leitinger et al. [LFMW14], using the ML principle. The maximum of the highly multi-modal likelihood function has to be found, which derives from the channel model introduced in Equation (3.6). In order to cope with the multi-modality, a hybrid probabilistic–heuristic approach is used that combines a sequential importance re-sampling (SIR) particle filter (PF) with the concept of particle swarm global optimisation (PSO). The performance of the algorithm was evaluated using real channel measurements for which an accuracy better than 3 cm has been obtained in 90% of the estimates (using only one active anchor, a pulse duration of $T_p = 0.5$ ns and $f_c = 7$ GHz). The results have shown that the knowledge of diffuse multipath significantly increases the performance of the positioning algorithm (see Figure 4 in Leitinger et al. [LFMW14]).

The above papers have assumed prior knowledge of a floor plan to compute the positions of the VAs, representing the geometry. In Leitinger et al. [LMLW15], a simultaneous localisation and mapping (SLAM) approach has been described that avoids this prior knowledge. The agent position and the VA positions are jointly estimated in a measurement-per-measurement manner. Only prior knowledge of the anchor positions is assumed. Here, the SINRs, the position-related information of the individual MPCs, are again used for estimating the agent position. Their estimation is also achieved during the position tracking. The position error performance virtually matches the performance of the method that assumes a known floor plan (see Figure 3 in Leitinger et al. [LMLW15]).

The paper by Kuang et al. [KAT13] present a structure-from-motion algorithm to simultaneously estimate the receiver motion, the transmitter position, and the positions of the corresponding VSs. The outcome of the structure-from-motion algorithm then serves as initial input for a non-linear least square algorithm to refine the estimated receiver, physical and virtual source (VS) positions. In comparison, a random sample consensus (RANSAC) approach for automatic matching of data has also been implemented and tested. Using real channel measurements over the whole-FCC bandwidth from 3.1 to 10.6 GHz both approaches were successfully tested resulting in an accuracy in the centimetrer region. Figure 3.21 shows the ground truth motion (red circles) and the estimated receiver positions (blue dots) and the directions to the source positions.

3.3.4.2 Non-UWB multipath-assited indoor tracking

All previous methods in this Section have in common that UWB signals are used for positioning. In Zhu et al. [ZVK^{+}15] the aim is to track user movements with accuracy down to centimeters using standard cellular bandwidths of 20–40 MHz by using the phase information of the MPCs and large antenna arrays to achieve separability. Using an EKF, the phases of
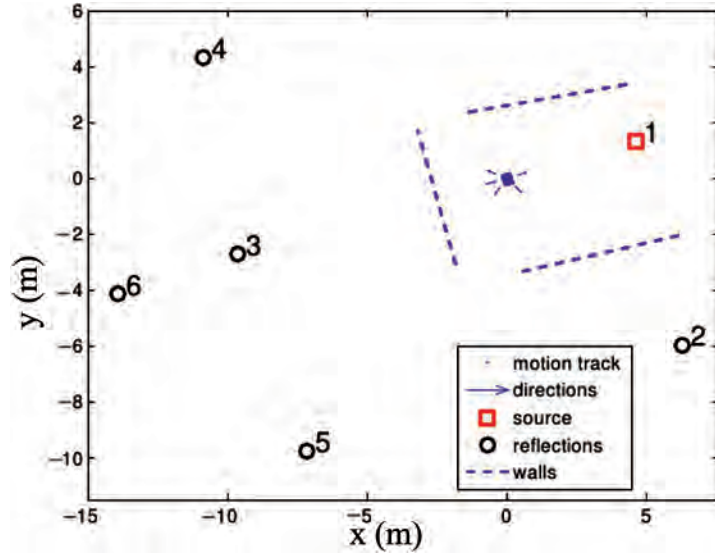

(a)

(b)
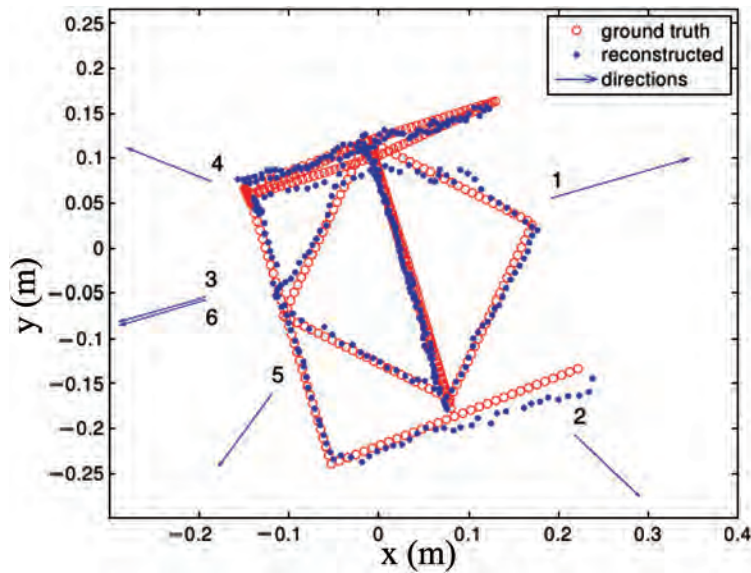
Figure 3.21   (a) Ground truth motion (*red circles*), the estimated receiver positions (*blue dots*) and the direction to the real and the virtual sources (VSs) positions. (b) Positions of the physical transmitter (red square), VSs (black circles), and hypothesised reflective wall positions based on the relative positions between physical transmitter and reflections.
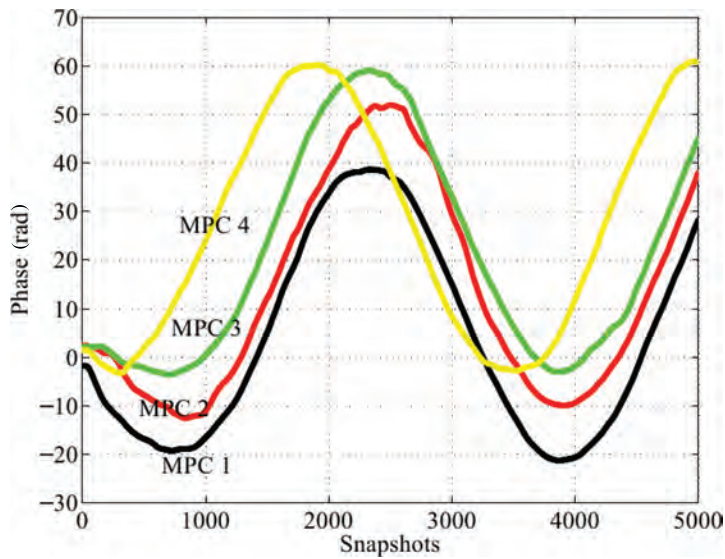

Figure 3.22   Tracked phases of a number of MPCs in circular movement measurements.

MPCs are estimated and tracked. The origins of the MPCs, the VA positions, and the according transmitter position and also the receiver position, are then estimated by translating the phase information into a propagation distance and using the structure-from-motion approach [KAT13]. By using the continuous behavior of the phases of the MPCs, a very high level of positioning accuracy is reached. In Figure 3.22 the tracked phases of a number of MPCs are shown for an agent (receiver) that moves on a circular trajectory (see Figure 1 in Zhu et al. [ZVK$^+$15]).